ACS Catalysis

Open Access

This article is licensed under CC-BY 4.0

pubs.acs.org/acscatalysis

Research Article

Elucidating the Role of Mo Vacancies in a Two-Dimensional Molybdenum Carbide MXene on Fischer–Tropsch Catalysis

Evgenia Kountoupi, Yevkeni Wisse, Mikhail Agrachev, Faidra Amargianou, Joseph Halim, Diana Piankova, Leiqiang Qin, Pierre Florian, Paula M. Abdala, Gunnar Jeschke, Tristan Petit, Vitaly V. Ordomsky, Christoph R. Müller, Johanna Rosen, and Alexey Fedorov*

Cite This: *ACS Catal.* 2026, 16, 14328–14346

Read Online

ACCESS | Metrics & More | Article Recommendations | Supporting Information

ABSTRACT: Bulk molybdenum carbides catalyze the Fischer–Tropsch (FT) reaction but display low selectivity to liquid hydrocarbons. Understanding which structural features of Mo carbide-based catalysts correlate with a selectivity to C_{5+} products requires detailed structure-performance studies. Here, we investigate the effect of Mo vacancies (V_{Mo}) on the FT performance of the two-dimensional (2D) *i*-MXene $Mo_{4/3}CT_x$, where T_x are the surface passivating groups. We show that the initially ordered V_{Mo} sites, constituting ca. one-third of all Mo sites in $Mo_{4/3}CT_x$, undergo clustering already at 250 °C under H_2. Following V_{Mo} clustering, lattice carbon is released as CH_4 and CO, creating carbon vacancies (V_C), which also form in $Mo_{4/3}CT_x$ under FT conditions at 330 °C. The presence of V_C sites is associated with a high selectivity towards methane and C_2–C_4 alkanes and a reduced selectivity for higher, C_{5+}, alkanes. $Mo_{4/3}CT_x$ converts CO at a rate of ca. 60–80 $mmol_{CO}$ $(g_{cat}\ h)^{-1}$, which is comparable to that of the T_x-free 2D-Mo_2C and 2D-Mo_2C_{1-x} reference catalysts that only contain a Mo^{+2} (carbidic) electronic state. However, post-FT analysis of $Mo_{4/3}CT_x$ shows that it contains Mo^{+2}, Mo^{+4}, and Mo^{+5} states, possibly because oxygen atoms populate the V_C sites and do not block the Mo^{+2} active sites at the surface. $Mo_{4/3}CT_x$ undergoes a phase transition to cubic α-MoC_{1-x} at 400 °C under H_2, which leads to a continuous deactivation under FT conditions, suggesting, more generally, that pretreatment protocols for MXenes should be carefully optimized to unlock their potential in thermal catalysis.

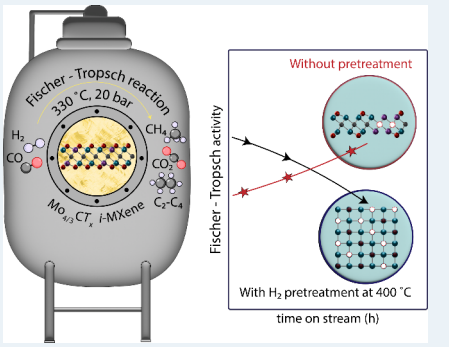

KEYWORDS: *2D molybdenum carbide, i-MXene catalysts, reductive defunctionalization, carbon vacancies, molybdenum vacancies, structure-performance relationships*

1. INTRODUCTION

The Fischer–Tropsch (FT) process enables the industrial production of synthetic fuels via the heterogeneous hydrogenation of CO, typically over iron or cobalt-based catalysts.[1−4] In the context of a sustainable economy, the reactants H_2 and CO can be obtained, respectively, from water electrolysis powered by renewable energy and from the reverse water gas shift reaction of air-captured CO_2.[5,6] The FT reaction (eq 1) is an exothermic polymerization reaction with a product distribution governed by Anderson–Schulz–Flory (ASF) statistics.[7−9] When carbon chain growth is slow, the undesired methanation, which is the most prominent competing reaction, prevails (eq 2).[10−12]

$$(2n+1)H_2 + nCO \rightarrow C_nH_{2n+2} + nH_2O,\ \Delta H^0_{298K} = -165\ kJ{\cdot}mol^{-1}_{CO} \quad (1)$$

$$3H_2 + CO \rightarrow CH_4 + H_2O,\ \Delta H^0_{298K} = -206\ kJ{\cdot}mol^{-1}_{CO} \quad (2)$$

Under FT conditions, zero-valent Fe and Co catalysts are frequently reported to transform into carbides,[13−15] whereby the FT activity, selectivity, and stability depend on the formation of the carbide phases and the extent of carbidization.[16−18] For instance, carbon-rich phases such as ε-Fe_2C have been shown to exhibit greater C–C coupling ability (i.e., lower methanation activity) relative to Fe^0, χ-Fe_5C_2, and χ-Fe_7C_3.[17−19] Furthermore, it has been suggested that the carbidic carbon (C^{carb}) of iron carbide is involved in the chain growth step, resulting in the formation of a carbon vacancy (V_C) at the carbon-terminated surface; carbon vacancies serve as CO adsorption and dissociation sites in a process that heals the V_C sites and restores the carbidic surface.[20−22]

Received: March 5, 2026
Revised: May 26, 2026
Accepted: May 27, 2026
Published: June 30, 2026

ACS Publications

© 2026 The Authors. Published by American Chemical Society

https://doi.org/10.1021/acscatal.6c01809
ACS Catal. 2026, 16, 14328–14346

Downloaded from pubs.acs.org/acscatal/article-pdf/16/15/14328/6529852/cs-2026-018095.pdf by LINKOPING UNIV user on 04 October 2026

A related family of FT catalysts is based on molybdenum carbides.[23−26] Compared to Fe carbides, Mo carbides exhibit a stronger stabilization of surface O* sites,[27,28] which facilitates CO activation.[29,30] However, a high oxygen adsorption energy can result in the blocking of the active Mo sites with surface O*, thereby lowering the catalytic activity.[31−33] That being said, comparable turnover frequencies in FT to those of χ-Fe_5C_2 have been reported for face-centered cubic (fcc) MoC_{1-x} and hexagonal close-packed (hcp) Mo_2C, viz., 0.06 s^{-1} at ca. 300 °C,[25,34] motivating further research on Mo carbide-based catalysts, given their advantages such as tolerance against sulfur impurities, which are present in fossil-based feedstocks and rapidly deactivate conventional Fe- and Co-based FT catalysts.[35,36] However, compared to Fe-based catalysts, molybdenum carbide catalysts have typically shown lower yields of C_{5+} alkanes, but higher yields of methane and C_2–C_4 alkanes at high CO conversions.[24,37] Since C_2=C_4 olefins are more prevalent at low CO conversions of <1%, it has been hypothesized that C_2–C_4 alkanes may form via secondary hydrogenation reactions.[25,38,39] A further disadvantage of catalysts based on Mo carbides is their high selectivity to CO_2 that can reach up to 50%.[37,40,41] This is due to the preferred removal of O*, formed due to the dissociation of CO on the carbidic surface sites, as CO_2 via a reaction with CO*.[42] In addition, CO_2 may originate from the competing water gas shift (WGS) reaction (i.e., CO + $H_2O \leftrightarrow CO_2 + H_2$).[25,43,44]

While the passivation of carbidic (i.e., Mo^{+2}) sites on a Mo_2C surface with O* is known to reduce the number of active sites and lower the catalytic activity,[24,25] the role of V_C sites on the FT activity and selectivity is less understood. For instance, under an H_2 atmosphere, carbidic carbon in a three-dimensional (3D) hcp-Mo_2C structure has been reported to be stable up to 400 °C; in contrast, when increasing the temperature to 500–650 °C, decarburization (via CH_4 formation) was observed.[41] No structural sensitivity was reported for the FT reaction over unsupported Mo carbides with hcp and fcc phases and different surface areas, presumably due to the in situ reconstruction of the catalyst surface.[25] Another study, however, showed that carbidic carbon-rich fcc-MoC_{1-x} is more active than hcp-Mo_2C, with respective TOFs of 0.055 and 0.036 s^{-1} at a CO conversion of 1.5%.[24] It was further observed that under FT conditions, the ratio of O : C^{carb} in these catalysts decreased, which was paralleled by increased activity.[24,45] Other studies have reported a decrease in the activity of Mo_2C catalysts with time on stream (TOS), attributed to the deposition of carbonaceous species.[25,41]

A key conclusion of studies exploring 3D Mo carbides as FT catalysts is that improving their productivity requires high specific surface areas in combination with an effective control over the C and O content (both on the surface and in the crystal lattice) during catalysis (Figure 1a).[46] In this context, two-dimensional (2D) model catalysts, i.e., MXenes,[47,48] including the multilayered crystalline 2D molybdenum carbide Mo_2CT_x,[49] can provide valuable insights into the interplay between the C and O stoichiometries in Mo carbide catalysts. In Mo_2CT_x, T_x denotes –O–, –OH, and –F (or –Cl) passivating groups that are bound to Mo sites. The carbon layer in Mo_2CT_x is sandwiched between two Mo layers; each carbon atom is octahedrally coordinated to Mo atoms. The interlayer distance between the nanosheets in multilayered crystalline Mo_2CT_x is ca. 0.5–1.0 nm and depends on the etching and

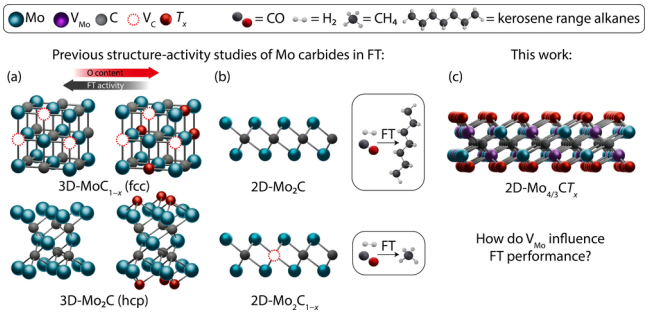

Figure 1. Selected results of FT structure-activity studies of (a) 3D fcc-MoC_{1-x} and hcp-Mo_2C with the influence of the oxygen content on the activity, (b) Mo_2CT_x MXene-derived catalysts 2D-Mo_2C and 2D-Mo_2C_{1-x} along with the influence of V_C sites on the selectivity towards higher alkanes, and c) the $Mo_{4/3}CT_x$ *i*-MXene structure with a research question of the present study.

pretreatment conditions, strongly influencing the accessibility of the interior sites to reactants.[50−52] MXenes, in particular Mo_2CT_x, have shown promising performance in a variety of catalytic applications, such as NH_3 synthesis,[50,53−55] CO_2 hydrogenation,[56] and alcohol hydrogenolysis.[57] Therefore, in-depth structure-performance studies on Mo MXenes can provide strategies for tailoring these highly tunable materials to further expand their potential in catalysis and the scope of their applications.

Under FT conditions, activated Mo_2CT_x produced liquid, higher alkanes (ASF value $\alpha = 0.87$) with a gravimetric rate of ca. 60 $mmol_{CO}$ $(g_{cat}\ h)^{-1}$ and a TOF_{CO} of 0.34 s^{-1} (C_{5+} alkanes were produced with a rate of 15.7 $mmol_{C5+}$ $(g_{cat}\ h)^{-1}$ and a product-specific TOF_{C5+} of 0.09 s^{-1}).[42] Such rates were achieved after the passivating groups of Mo_2CT_x were reductively defunctionalized, partially after H_2 pretreatment at 400 °C and fully after in situ reductive defunctionalization under FT conditions (330 °C, H_2:CO = 2:1), yielding a T_x-free 2D-Mo_2C state.[42,56] However, when compared to the reference 3D hcp-Mo_2C (β polymorph) on a per-site basis (i.e., TOF), the rate of CO consumption is only ca. 3 times higher for 2D-Mo_2C. In contrast, the yield of higher alkanes normalized per gram of catalyst is higher by two orders of magnitude, highlighting the advantage of 2D-Mo_2C over 3D-Mo_2C catalysts. When the reductive defunctionalization is performed under H_2 at a temperature of 500 °C, a T_x-free material 2D-Mo_2C_{1-x} forms, characterized by the presence of V_C sites. In contrast to 2D-Mo_2C, 2D-Mo_2C_{1-x} is selective to methane under FT conditions, reducing the gravimetric rate of formation of C_{5+} alkanes to only 0.6 $mmol_{C5+}$ $(g_{cat}\ h)^{-1}$ and TOF_{C5+} of 0.004 s^{-1} (Figure 1b).[42] This result contrasts with a previous report that suggested V_C in a 3D Mo oxycarbide to favour chain growth rather than methanation.[23]

However, it should be noted that Mo_2CT_x, with its high theoretical surface area of ca. 285 $m^2\ g^{-1}$ (eq S1), and in the absence of passivating T_x groups, features a theoretical CO adsorption site density of about 4.7 sites per nm^{-2} (assuming one CO chemisorbs on a threefold hollow site, see SI for details). This corresponds to a theoretical CO capacity of 2D-Mo_2C of ca. 2223 μmol g_{cat}^{-1}, when assuming that all Mo sites are carbidic and accessible. However, when measured by pulsed CO chemisorption at –30 °C, the CO capacity of 2D-Mo_2C_{1-x} is only 47 μmol g_{cat}^{-1},[42] which is ca. 50 times lower than the theoretical value. This

Downloaded from pubs.acs.org/acscatal/article-pdf/16/15/14328/6529852/cs-2026-018095.pdf by LINKOPING UNIV user on 04 October 2026

https://doi.org/10.1021/acscatal.6c01809
ACS Catal. 2026, 16, 14328−14346

comparison underscores the pronounced inaccessibility of Mo sites in crystalline multilayered 2D-Mo_2C MXene,[50,52,56] arising from the low pore size (i.e., the shortest Mo–Mo interlayer distance) of ca. 0.5–1.0 nm.[58] Another characteristic feature of multilayered MXenes, such as Mo_2CT_x, is the difference in the amounts of T_x groups on the exterior and interior layers in the crystalline stack of MXene nanosheets. That is, Mo sites in the exterior layers, probed by surface-sensitive methods such as X-ray photoelectron spectroscopy (XPS), are either more oxidized or reduced under air or after H_2 treatment, respectively, relative to Mo sites probed by an integral method, such as X-ray absorption near edge structure (XANES).[50] Limited accessibility into the interlayer space likely enhances the differences in spatially varying composition between the interior and exterior layers; in addition, the exterior layers are more disordered, which may further contribute to the observed differences in the coverages of the T_x groups.[50]

Structural defects in general, and point defects in particular (such as vacancies), are common in low-dimensional solid materials, including nanosheets and nanoparticles, due to their high surface energy.[59] Furthermore, point defects can alter the electronic and geometric structures of the host material, thereby changing its catalytic properties.[60,61] For example, cation vacancies have been shown to play a role in the replenishment of the lattice oxygen atoms in an oxide catalyst and to facilitate propylene epoxidation.[62] However, the deconvolution of structure–property relationships in defective structures and disordered layered materials is challenging because it is difficult to introduce and characterize defect types in a controlled manner, and because defects evolve under reaction conditions.[60] One such material with controlled defect positions is a Mo carbide *i*-MXene containing Mo vacancies (V_{Mo}) with in-plane ordering at one-third of its Mo sites, i.e., $Mo_{4/3}CT_x$.[63,64] To the best of our knowledge, the effect of Mo vacancies in Mo carbides on FT catalysis remains unexplored, making $Mo_{4/3}CT_x$ a suitable model catalyst (Figure 1c).

In this work, we probe the influence of Mo vacancies in the catalytic performance of Mo MXenes under high temperature Fischer–Tropsch conditions (330 °C, CO:H_2 = 1:2, 20 bar). For this purpose, we explore the dynamic interplay between the Mo, C, and O stoichiometries of $Mo_{4/3}CT_x$ *i*-MXene both under H_2 treatment and FT conditions. We show that the V_{Mo} sites appreciably decrease the stability of C^{carb} in the *i*-MXene lattice under reducing conditions. Specifically, C^{carb} leaves the structure as CH_4 and CO under H_2 treatment already at 250 °C (1 bar) or under FT conditions. The formation of V_C sites follows the clustering of V_{Mo} sites. The onset of the 2D-to-3D phase transformation for $Mo_{4/3}CT_x$ is about 400 °C for forming α-MoC_{1-x}; subsequently, α-MoC_{1-x} transforms to β-Mo_2C at about 600 °C. Since $Mo_{4/3}CT_x$ contains oxidized Mo sites at 400 °C under H_2, T_x-free 2D-$Mo_{4/3}C_{1-x}$ cannot be prepared in a phase-pure form via H_2 treatment. The poor reducibility of $Mo_{4/3}CT_x$-derived catalysts keeps them oxidized under FT conditions. Despite the more oxidized state of Mo, $Mo_{4/3}CT_x$ displays CO consumption rates similar to those of 2D-Mo_2C, providing indirect evidence that O populates the subsurface without blocking the active sites. $Mo_{4/3}CT_x$ is primarily a methanation catalyst with a reduced ability for C–C coupling, limited to C_2–C_4 products, which we attribute to the presence of V_C sites under FT conditions. The structure of Mo sites and the catalyst's stability are sensitive to the specific reductive conditions applied (H_2 or CO:H_2), with a non-H_2-treated $Mo_{4/3}CT_x$ reaching a higher reaction rate with time on stream than the H_2-treated $Mo_{4/3}CT_x$, which transforms into α-MoC_{1-x} and deactivates under FT conditions.

2. MATERIALS AND METHODS

2.1. Materials

Delaminated $Mo_{4/3}CT_x$ was prepared from $(Mo_{2/3}Sc_{1/3})_2AlC$ by a previously reported method.[63,64] To prepare $(Mo_{2/3}Sc_{1/3})_2AlC$, a stoichiometric amount of graphite, Mo, Al, and Sc was annealed in a tube furnace under a flow of Ar for 24 h at 1550 °C. The resulting $(Mo_{2/3}Sc_{1/3})_2AlC$ was sieved and treated with 48% HF at room temperature for 1 day. The obtained $Mo_{4/3}CT_x$ powder was intercalated with tetrabutylammonium hydroxide (TBAOH) to prepare a suspension of single and few-layered nanosheets. The suspension was freeze-dried to yield a solid $Mo_{4/3}CT_x$, which was ground into a powder.

The reference multilayered (i.e., non-delaminated) Cl-terminated Mo_2CT_x was prepared by treating commercial Mo_2Ga_2C (Laizhou Kai Kai Ceramic Materials Co., Ltd) with 37% HCl (Fischer Scientific, for trace metal analysis) at 180 °C for 4 days in a sealed autoclave, followed by washing with deionized water until a pH of ca. 6 was reached (4 × 40 mL washings). The obtained powder was dried in air at 80 °C overnight. The reference multilayered F-terminated Mo_2CT_x was prepared using HF, as reported previously.[56] Mo_2Ga_2C used to prepare delaminated Mo_2CT_x was obtained by annealing layers of Mo_2C and molten Ga in a tube furnace under a flow of Ar to 800 °C for 72 h, followed by HCl treatment to remove excess Ga.[49] The obtained Mo_2Ga_2C was treated with 48% HF at 35 °C for 5 days to obtain Mo_2CT_x, which was delaminated with TBAOH as described above. The synthesis protocols are described in further detail in the SI file. The references β-Mo_2C (99.5% purity), MoO_2 (99% purity), and MoO_3 (≥99.5% purity) were purchased from Sigma-Aldrich.

2.2. Characterization Details

Ex situ X-ray total scattering experiments were conducted at the beamline ID31 of the European Synchrotron Radiation Facility (ESRF). The X-ray diffraction (XRD) patterns and X-ray pair distribution functions (PDFs) of the activated and post-reaction catalysts were obtained without exposure of the activated specimen to air. X-ray absorption spectroscopy (XAS) measurements at the Mo K-edge were conducted at the beamline BM31 of ESRF. The measurements included the collection of XANES and extended X-ray absorption fine structure (EXAFS) data, both ex situ and in situ during a H_2 temperature programmed reduction (TPR) experiment. During this in situ H_2-TPR experiment, we additionally collected XRD and PDF profiles, as well as mass spectra (MS) of the effluent gas. Electron paramagnetic resonance (EPR) and XPS data were collected from the activated and post-reaction catalysts without exposure to air, using sealed capillaries or an air-tight transfer cell, respectively. Transmission electron microscopy (TEM) and scanning electron microscopy (SEM) were performed on the air-exposed materials. Soft XAS measurements at the O K-, C K-, and Mo $M_{2,3}$-edges of the delaminated $Mo_{4/3}CT_x$ and Mo_2CT_x were acquired in transmission mode in a scanning transmission X-ray microscope (STXM) at the MYSTIIC endstation of the EMIL beamline at BESSY II. Further characterization details are provided in the SI file.

2.3. Catalytic Testing

The catalytic performance of $Mo_{4/3}CT_x$ and the reference β-Mo_2C in CO hydrogenation was evaluated in a fixed-bed reactor. The catalyst powder (100–350 mg) was placed between plugs of quartz wool in a

Downloaded from pubs.acs.org/acscatal/article-pdf/16/15/14328/6529852/cs-2026-018095.pdf by LINKOPING UNIV user on 04 October 2026

https://doi.org/10.1021/acscatal.6c01809
ACS Catal. 2026, 16, 14328–14346

stainless-steel reactor with an internal diameter of 4.57 mm. If a H_2 pretreatment step was applied, the catalyst was exposed to undiluted H_2 (20 mL min^{-1}) at 400 °C (ramping rate was 5 °C min^{-1}) for 2 h. After pretreatment, the reactor temperature was decreased to 170 °C, and syngas (ca. CO:H_2 = 1:2 mixture with 5.3 mL min^{-1} of CO and 11.3 mL min^{-1} H_2) was introduced at a weight hourly space velocity (WHSV) of 10.0 L $(g_{cat}\ h)^{-1}$ and 2.8 L $(g_{cat}\ h)^{-1}$ for the $Mo_{4/3}CT_x$ catalysts and reference β-Mo_2C, respectively. The CO gas bottle contained 5% N_2, which served as an internal standard. Next, the pressure was increased to 20 bar, and the reaction temperature was increased to 330 °C. The reaction products were analysed with an on-stream Bruker 450 Gas Chromatograph (GC) equipped with a thermal conductivity detector (TCD) and a flame ionisation detector (FID). Two separate columns were used for the analysis: a packed CTR 1 column and an Rt-Q-PLOT capillary column connected to the TCD and FID, respectively. The time zero of the time on stream scale corresponds to the first GC point taken after reaching 330 °C.

The post-reaction $Mo_{4/3}CT_x$ catalysts were recovered in a glovebox for characterization and, unless stated otherwise, handled without exposure to air.

3. RESULTS

3.1. Characterization of $Mo_{4/3}CT_x$

A representation of the atomic structure of vacancy-ordered $Mo_{4/3}CT_x$ *i*-MXene is shown in Figures 2a and S1, where T_x groups are omitted for clarity. The ordering of V_{Mo} in $Mo_{4/3}CT_x$ is caused by the in-plane ordering of the Sc atoms in the parent $(Mo_{2/3}Sc_{1/3})_2AlC$ phase; the removal of Sc (and Al) by HF treatment retains this ordering of Mo atoms, i.e., it yields ordered Mo vacancies.[63,64] According to inductively coupled plasma optical emission spectrometry (ICP-OES) analysis, the

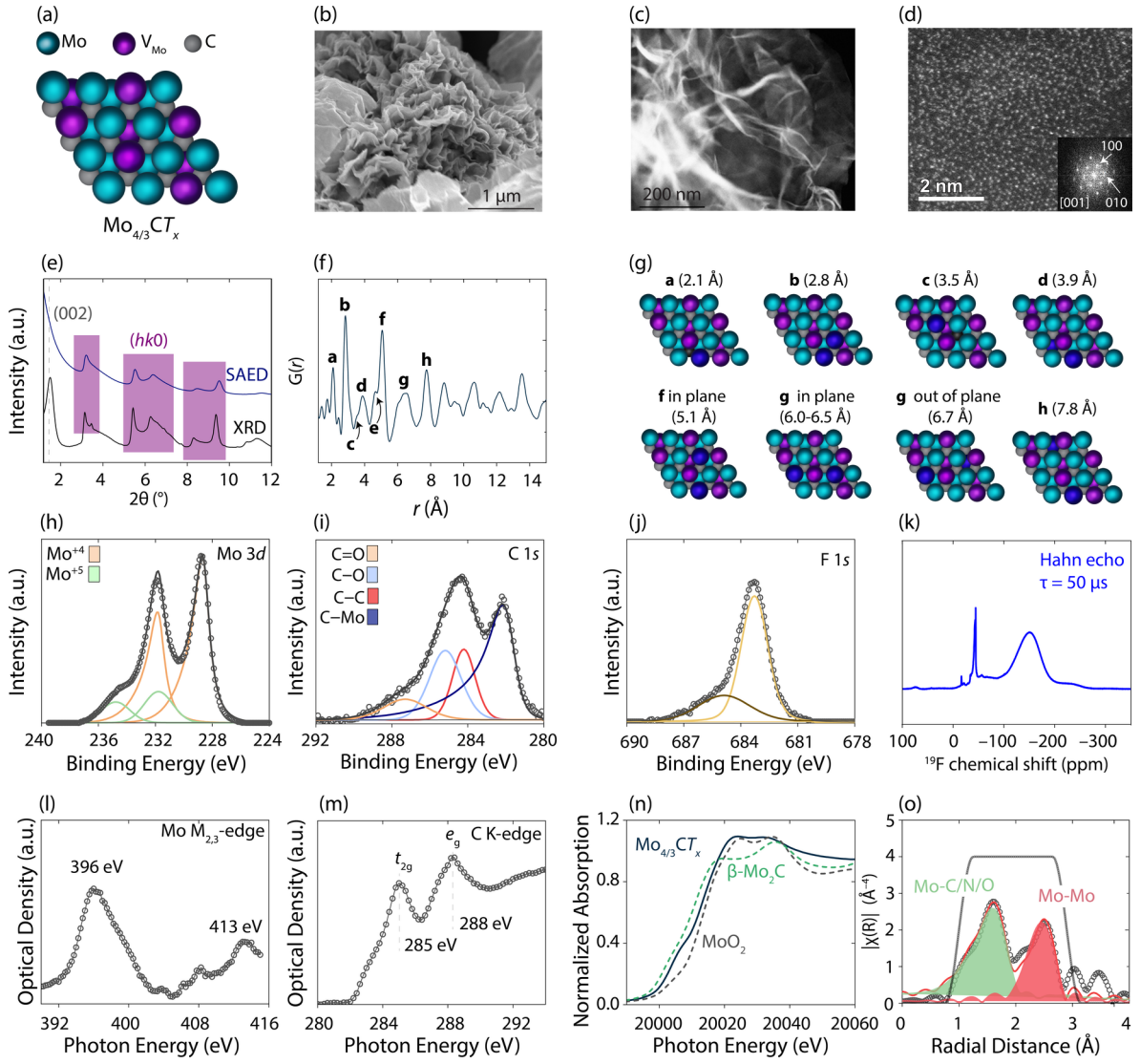

Figure 2. (a) A representation of the atomic structure of vacancy-ordered $Mo_{4/3}CT_x$ with (b) SEM image, (c) HAADF-STEM image, (d) high-resolution HAADF-STEM image with the corresponding FFT pattern in the inset, (e) XRD pattern compared to the integrated 1D profile obtained from the SAED pattern, (f) PDF profile, (g) selected identified interatomic distances of the PDF profile, (h) Mo 3*d*, (i) C 1*s*, and (j) F 1*s* XPS regions, (k) ^{19}F MAS NMR spectrum, (l) Mo $M_{2,3}$-edge, (m) C K-edge, (n) Mo K-edge XANES profile along with that of the references β-Mo_2C and MoO_2 (dashed lines), and (o) the fitted EXAFS profile of $Mo_{4/3}CT_x$. The passivating T_x groups in the structures in panels (a) and (g) are omitted for clarity.

Downloaded from pubs.acs.org/acscatal/article-pdf/16/15/14328/6529852/cs-2026-018095.pdf by LINKOPING UNIV user on 04 October 2026

https://doi.org/10.1021/acscatal.6c01809
ACS Catal. 2026, 16, 14328−14346

Mo weight content in $Mo_{4/3}CT_x$ is 65%; minor amounts of Sc and Al (0.4% w/w and 1.7% w/w, respectively) were additionally detected. SEM images presented in Figures 2b and S2–S4 demonstrate a disordered, loosely aggregated network of curved $Mo_{4/3}CT_x$ sheets. The morphology, nano- and atomic structure of the as-prepared $Mo_{4/3}CT_x$ were further analyzed using scanning transmission electron microscopy (STEM). As seen from the overview high-angle annular dark-field (HAADF)-STEM image in Figure 2c and in Figures S5 and S6, the morphology of the *i*-MXene flakes resembles wrinkled paper, formed during freeze-drying of the ink containing the delaminated $Mo_{4/3}CT_x$ flakes.

A high-resolution HAADF-STEM image shown in Figure 2d was acquired at the flake edge, which allowed the regions of lower and higher Mo contrast to be revealed. A corresponding fast Fourier transform (FFT) pattern obtained from the same area can be indexed to Mo_2CT_x MXene with an ABC stacking oriented along the [001] zone axis (Figure 2d, inset). The FFT indexing, together with the contrast variations, suggests that the long-range vacancy ordering in $Mo_{4/3}CT_x$ is locally disrupted at the flake edges, leading to the formation of Mo_2CT_x-like domains and areas with clustered V_{Mo}. This morphology resembles that reported for $Nb_{1.33}CT_x$,[65] which has the same number of metal vacancy sites as in $Mo_{4/3}CT_x$ but lacks vacancy ordering. While ordered V_{Mo} sites have been visualized in $Mo_{4/3}CT_x$ previously,[63] the local loss of ordering in $Mo_{4/3}CT_x$ may be induced by beam damage at high magnification and/or by differences in specimen preparation. In contrast to direct deposition of an $Mo_{4/3}CT_x$ suspension of single- and few-layer flakes, the suspension was dried in the present work, the resulting powder was mechanically ground, and then deposited onto the TEM grid. The HAADF image additionally identified areas of low Mo contrast (voids) with an average diameter of 0.9 ± 0.4 nm (Figure S7). This microstructure likely originates from the beam-induced clustering of the V_{Mo} sites, creating thereby Mo_2CT_x-like domains.[66] These results indicate a propensity of $Mo_{4/3}CT_x$ to undergo structural changes, as discussed in detail below.

The integrated 1D profile from selected area electron diffraction (SAED) acquired on a thin flake shows mainly *hk*0 reflections when indexing using space group $P6_3/mmc$ (Figure 2e). The lack of the (002) reflection indicates that the $Mo_{4/3}CT_x$ nanosheets were delaminated and subsequently reassembled with a disordered stacking. The XRD profile of $Mo_{4/3}CT_x$ presented in Figure 2e features the (002) reflection at ca. 1.5° (wavelength of incident radiation λ = 0.24 Å). The peak's low intensity compared to crystalline, multilayered MXenes suggests a poor stacking coherence, which may also be associated with hydration heterogeneities (Figure S15).[67] The *c* parameter of 19 Å suggests the shortest distance between two Mo atoms in neighboring nanosheets is ca. 7 Å. A series of additional peaks at 3.1°, 5.4°, 6.3°, and 9.4° is ascribed mainly to *hk*0 reflections due to in-plane ordering.[68,69] The high-angle tailing of these reflections suggests turbostratic disorder in the *z*-axis direction,[70−72] consistent with the SAED-derived results. Since the (002) XRD peak in the delaminated $Mo_{4/3}CT_x$ used in this work corresponds to a *c* lattice parameter of 19 Å, which is notably lower than the ca. 36 Å value reported for delaminated $Mo_{4/3}$ CT_x containing TBA^+ ions between the layers,[73] the presence of TBA^+ ions in $Mo_{4/3}CT_x$ used in this work is unlikely.

The PDF of the X-ray total scattering data, represented by $G(r)$, is shown for $Mo_{4/3}CT_x$ in Figure 2f. The peak assignment is based on the DFT-derived, relaxed atomic structure of 2D-$Mo_{4/3}C(O)_{2/3}(F)_{4/3}$ (see Table S1) as well as previously reported PDF analyses of Mo_2CT_x and $Mo_2(C,N)T_x$ MXenes (Figure S8).[50,64,74] Selected interatomic distances in the low *r*-region of the PDF profile are visualized in Figure 2g, where Mo–Mo pairs are depicted in dark blue and Mo–C pairs in dark blue and black. Peaks marked as **a**, **c**, and **e** at 2.1, 3.5, and 4.6 Å correspond, respectively, to the first, second, and third nearest Mo–C pairs (Figures 2g and S8). The peak at 2.8 Å, denoted as **b**, represents the nearest Mo–Mo pairs, suggesting similar interatomic distances when the atoms are located in the same (in-plane) or opposite (out-of-plane) Mo layers of the same nanosheet. The feature **d** at 3.9 Å corresponds to the second nearest out-of-plane Mo–Mo pairs. The feature **f** at 5.1 Å corresponds to the second nearest in-plane or third nearest out-of-plane Mo–Mo pairs. The broad feature, **g**, centered at ca. 6.3 Å, corresponds to Mo–Mo pairs located on either side of the vacancy (both in-plane and out-of-plane). The broadness of this feature is attributed to the distribution of distances between atomic pairs around the V_{Mo} site, with the distance of a given pair depending on its orientation relative to the vacancy site. Finally, the feature **h** at 7.8 Å represents the distance between the fifth nearest out-of-plane Mo–Mo pairs.

The surface elemental composition and electronic states of $Mo_{4/3}CT_x$ were probed by XPS (see Figure S9 for the valence band spectrum and Table S2 for the atomic ratios). Fitting of the Mo 3*d* region identified two chemical states, i.e., one Mo $3d_{5/2}$ component with a binding energy (BE) of 228.7 eV and another component at 231.8 eV (Figure 2h and Table S3). The relative intensities of these states, assigned, respectively, to Mo^{+4} and Mo^{+5} sites in $Mo_{4/3}CT_x$ were 81 and 19%. Thus, the surface sites in $Mo_{4/3}CT_x$ are completely passivated by T_x surface groups, which is typical for as-prepared Mo MXenes.[49,63,64,75] It has been reported that the Ti $3p_{3/2}$ binding energy in a $Ti_3C_2T_x$ MXene is higher for oxo (–O–) T_x groups relative to–F/OH groups.[76] Therefore, the lower BE component in the spectrum of $Mo_{4/3}CT_x$ (ca. 229 eV) may be linked to Mo–F/OH sites, while the higher BE component at ca. 232 eV is linked to Mo-μ^2-O sites, qualitatively explaining the lower fraction of the specific Mo state at a BE of ca. 232 eV in $Mo_{4/3}CT_x$ relative to Mo_2CT_x, as Mo_2CT_x has a higher and lower population of –O– and –F groups, respectively. In addition, local disorder in $Mo_{4/3}CT_x$ around V_{Mo} sites distorts the coordination geometry of the T_x groups, potentially influencing the observed BE values.[64,76] The average Mo oxidation state, based on the fitting of the Mo 3*d* region of $Mo_{4/3}CT_x$, is approximately +4.2. The fitting of the C 1*s* XP spectrum is presented in Figure 2i, and the fitting details are provided in Table S4. The atomic ratio between Mo (i.e., combined Mo^{+4} and Mo^{+5} states) and the fitted carbidic carbon is 1.4, which is close to the nominal value of 1.33. The fitting of the F 1*s* region displays two components: a broad peak centered at 684.9 eV and a more intense, sharp peak with a maximum at 683.3 eV, indicating the presence of two distinct fluorine environments (Figure 2j and Table S5). This inference is consistent with the ^{19}F MAS NMR measurement, which shows two features, i.e., a broad peak at approximately –150 ppm and a sharp peak at approximately –45 ppm (Figure 2k). Analysis of the O 1*s* XPS region (Table S5) indicates, when considering the XPS features of the other regions, that the near-surface composition of $Mo_{4/3}CT_x$ is represented by the formula

Downloaded from pubs.acs.org/acscatsc/article-pdf/16/15/14328/6529852/cs-2026-018095.pdf by LINKOPING UNIV user on 04 October 2026

https://doi.org/10.1021/acscatal.6c01809
ACS Catal. 2026, 16, 14328−14346

$(Mo_{1.4}C_{1.0})(O_{0.5}OH_{0.7}F_{1.1})$ (see Figures S10 and S11). It is noted that although the ICP-OES analysis detected minor amounts of residual Al or Sc, the peaks of these elements were not observed in the XPS data and therefore Al and Sc are not expected to influence the catalytically relevant MXene sites residing at the exterior surface (Figure S10).

The electronic states of Mo, O, and C in $Mo_{4/3}CT_x$ were further examined with soft X-rays at the O K-, C K-, and Mo $M_{2,3}$-edges in a STXM experiment. The Mo $M_{2,3}$-edge spectrum of $Mo_{4/3}CT_x$ (Figure 2l) features the characteristic M_3 and M_2 peaks centered at 396 and 413 eV, respectively, due to the transitions from the $3p_{3/2}$ and $3p_{1/2}$ to the unoccupied 4*d* orbitals.[77] The position of the M_3 peak of $Mo_{4/3}CT_x$ is between the reported values of Mo^0 and MoO_2 (395 and 397 eV, respectively).[78,79] The t_{2g} and e_g splitting of the *p*-*d* hybridized orbitals was not resolved in the M_3 peak, in line with previous reports.[80] Turning to the C K-edge spectrum of $Mo_{4/3}CT_x$, intense peaks are observed at 285 and 288 eV (Figure 2m). Such peak positions are similar to those reported for 3D-Mo_2C, although the relative peak intensities differ between $Mo_{4/3}CT_x$ and 3D-Mo_2C.[81,82] In transition metal carbides with octahedrally coordinated carbon atoms, the latter two peaks are typically ascribed to transitions of C 1*s* electrons to the *p*-*d* (t_{2g}) and *p*-*d* (e_g) hybridized orbitals, respectively.[79] Because the carbon atoms in $Mo_{4/3}CT_x$ adopt a distorted octahedral coordination, further splitting of the t_{2g} set is expected; however, this was not resolved.[64,83,84] The O K-edge spectrum is presented in Figure S12 and shows two sharp peaks at 531.4 and 535.8 eV that are ascribed to the transition from the O 1*s* to the O 2*p* – Mo 4*d* unoccupied orbitals, while the broad peak between 540 and 545 eV is ascribed to the transition from O 1*s* to the O 2*p* – Mo 5*sp* hybridized orbitals.[85−87]

In contrast to surface-sensitive XPS, Mo K-edge XANES is an integral method that allows for probing the electronic states of Mo sites. Figure 2n displays the Mo K-edge XANES profiles of $Mo_{4/3}CT_x$ and selected references (β-Mo_2C, MoO_2). These spectra rely on hard X-rays that excite transitions from the 1*s* orbital to unoccupied 5*p* orbitals and states above the Fermi level. The determined edge energy of $Mo_{4/3}CT_x$ is ca. 20,010 eV, which is between that of β-Mo_2C and MoO_2 (ca. 20,008 and 20,012 eV, respectively). Assuming +2 and +4 oxidation states of Mo for β-Mo_2C and MoO_2, respectively, and a linear variation of oxidation state with edge energy, the average oxidation state of all Mo atoms (i.e., exterior and interior Mo atoms) in $Mo_{4/3}CT_x$ is ca. +3.[88] The difference between XPS and the Mo K-edge XANES-derived oxidation state of Mo is explained by a higher fraction of more oxidized Mo sites in the exterior layers probed by XPS relative to re-stacked multilayered $Mo_{4/3}CT_x$, where interior, less oxidized layers contribute more to the averaged XANES signal.[50]

The local coordination environment of Mo sites was then assessed with EXAFS. The fitting of the Fourier transform of the EXAFS function of $Mo_{4/3}CT_x$ is shown in Figure 2o. The Mo–C/T_x and Mo–Mo shells are observed at ca. 1.6 and 2.5 Å, respectively. The magnitude of the EXAFS function, $|\chi(R)|$, for both the Mo–C/T_x and Mo–Mo shells is very low (Figure S13). This can be attributed to the structural distortion and the distribution of interatomic distances in $Mo_{4/3}CT_x$, as predicted computationally,[64] leading to destructive interference and an appreciably decreased $|\chi(R)|$.[89,90] The intensity of the Mo–Mo peak is significantly lower than that of the Mo–C/T_x peak, consistent with the presence of metal vacancies.[69,91] The Fourier transform of the EXAFS function in the range k = 3.4–12 $Å^{-1}$ can be fitted by a model structure consisting of two layers of the elementary Mo_4C_3 structure with a *c* parameter of 19 Å. The EXAFS fitting in *k* space is provided in Figure S14, and the fitted average interatomic distances, coordination numbers (CN), and Debye–Waller factors (σ^2, the mean square variation in interatomic distances), are presented in Table 1. In particular, the Mo–C/T_x shell was fitted with a distance of 2.14(1) Å and a CN of 8(2) (Table 1, entry 1). The Mo–Mo shell was fitted with a distance of 2.83(1) Å and with a CN of 2(1).

3.2. Comparison of $Mo_{4/3}CT_x$ with the Reference Mo_2CT_x

In the following, we highlight key differences between delaminated and re-stacked $Mo_{4/3}CT_x$, crystalline multilayered Mo_2CT_x, and delaminated and re-stacked Mo_2CT_x (denoted *m*-Mo_2CT_x and *d*-Mo_2CT_x, respectively). XRD and SAED indicate strong tailing for the reflections associated with the *xy* plane, suggesting more pronounced turbostratic disorder in $Mo_{4/3}CT_x$ relative to *m*-Mo_2CT_x (see discussion after Figure S15 for details). The higher structural disorder of $Mo_{4/3}CT_x$ compared to *m*-Mo_2CT_x is evident by the broadening of features and loss of fine structure of the PDF peaks above ca. 3.5 Å (Figure S16). Additionally, EXAFS fittings indicate that the σ^2 values of $Mo_{4/3}CT_x$ (0.010 $Å^2$ for the Mo–Mo shell and 0.013 $Å^2$ for the Mo–C/T_x shell) are considerably higher compared to the ones reported for *m*-Mo_2CT_x (0.003 and 0.002 $Å^2$, respectively).[52] These observations show that $Mo_{4/3}CT_x$ is disordered both locally and in the long range.

All spectroscopic methods applied here indicate a lower oxidation state of Mo in $Mo_{4/3}CT_x$ than in the Mo_2CT_x references. More specifically, the average oxidation state of Mo in $Mo_{4/3}CT_x$, as determined by fitting of the Mo 3*d* XPS region,

Table 1. Mo K-edge EXAFS Fitting Results of $Mo_{4/3}CT_x$, $Mo_{4/3}CT_{x-400}$, and $Mo_{4/3}CT_{x-800}$[a]

entry	material	shell	CN	σ^2($Å^2$)	Δ*E*(eV)	*R* (Å)	*R* factor
1	$Mo_{4/3}CT_x$	Mo–C/T_x	8(2)	0.013(3)	−7(2)	2.14(1)	0.012
		Mo–Mo	2(1)	0.010(2)		2.83(1)	
2	$Mo_{4/3}CT_{x-400}$	Mo–C/T_x	8(1)	0.011(1)	−9(2)	2.11(1)	0.047
		Mo–Mo	4(2)	0.016(3)		2.92(2)	
3	$Mo_{4/3}CT_{x-800}$	Mo–C	4(1)	0.005(2)	−10(1)	2.09(1)	0.013
		Mo–Mo	11(1)	0.006(0)		2.97(1)	
4	β-Mo_2C	Mo–C	3*	0.003(2)	5(1)	2.08(1)	0.08
		Mo–Mo	12*	0.006(1)		2.98(1)	

[a]The S_0^2 value of 0.85 was determined by fixing the CN during the fitting of the β-Mo_2C reference (labelled *).

https://doi.org/10.1021/acscatal.6c01809
ACS Catal. 2026, 16, 14328−14346

Downloaded from pubs.acs.org/acscatal/article-pdf/16/15/14328/6529852/cs-2026-018095.pdf by LINKOPING UNIV user on 04 October 2026

is +4.2. In comparison, the average Mo oxidation states based on Mo 3*d* XPS in *m*-Mo_2CT_x is ca. +4.5.[56,92] The Mo M_3-edge is shifted by ca. 1 eV to higher energies for *d*-Mo_2CT_x compared to $Mo_{4/3}CT_x$ (Figure S17).[78,80,88] Similarly, when using Mo K-edge XANES analysis, which, unlike XPS analysis, is not skewed toward exterior Mo atoms, $Mo_{4/3}CT_x$ and *m*-Mo_2CT_x are found to have an average Mo oxidation state of ca. +3 and +4 (Figure S18). Furthermore, the white line intensity in the Mo K-edge spectrum of $Mo_{4/3}CT_x$ is considerably lower compared to that of *m*-Mo_2CT_x. The lower oxidation state of Mo in $Mo_{4/3}CT_x$ compared to Mo_2CT_x materials is a consequence of the distinct compositions of the T_x groups, as discussed below.

Comparison of the C 1*s* XPS data demonstrates that the BE of the carbidic carbon in $Mo_{4/3}CT_x$ is 0.5 eV lower than in Mo_2CT_x (282.0 eV and 282.5 eV, respectively, see Figure S19). The C K-edge spectrum *d*-Mo_2CT_x indicates a higher e_g : t_{2g} peak ratio compared to $Mo_{4/3}CT_x$ in line with a lower *d* band filling in *d*-Mo_2CT_x compared to $Mo_{4/3}CT_x$ (Figure S20).[93] The markedly decreased intensity of the peak at 531.6 eV in the O K-edge of $Mo_{4/3}CT_x$ relative to that for Mo_2CT_x could reflect the lower oxidation state of Mo due to Mo–O hybridization (Figure S12).[94] Deviations from the octahedral symmetry due to point defects in $Mo_{4/3}CT_x$ can induce a broadening of the peaks in the O K-edge spectrum of $Mo_{4/3}CT_x$ relative to Mo_2CT_x.[83,84]

The observed differences in the electronic states of Mo and carbidic carbon between HF-washed $Mo_{4/3}CT_x$ and previously published F-terminated *m*-Mo_2CT_x are attributed to the distinct relative amounts and distribution of functional groups.[42] According to the XPS-derived compositions $(Mo_{1.4}C_{1.0})(O_{0.5}OH_{0.7}F_{1.1})$ and $(Mo_{2.0}C_{1.0})(O_{1.8}OH_{0.8}F_{0.1})$,[42] the amount of divalent oxo groups in $Mo_{4/3}CT_x$ is approximately 3.5 times lower than in *m*-Mo_2CT_x, offset by a ca. 10 times higher amount of monovalent fluoride surface termination groups (Figure S11). The amount of monovalent hydroxy (–OH) groups is similar in both materials, leading to a T_x : Mo ratio of ca. 1.6 and 1.3 in $Mo_{4/3}CT_x$ and Mo_2CT_x, respectively. This trend qualitatively agrees with the fitted first-sphere coordination numbers in $Mo_{4/3}CT_x$ and Mo_2CT_x, which are 8(2) and 7(1), respectively.[52] Thus, compared to Mo_2CT_x, the presence of Mo vacancies in $Mo_{4/3}CT_x$ leads to a slightly higher number of T_x groups per Mo atom, which are mostly monovalent (bridging) fluoride functional groups. The fluoride T_x groups display two peaks in the F 1*s* XPS region (at a ca. 3:1 relative ratio), and two sites are also observed in the ^{19}F MAS NMR spectrum of $Mo_{4/3}CT_x$. This is in contrast to the F 1*s* XPS data of *m*-Mo_2CT_x, which shows a single peak (Figure S21a); likewise, the ^{19}F MAS NMR spectrum of *m*-Mo_2CT_x features a single site, accounting for ca. 99% of the signal (Figure S22). We relate the presence of two Mo–F environments in the XPS data of $Mo_{4/3}CT_x$ to V_{Mo} sites; i.e., the two F terminations could be either more proximal or more distant from a V_{Mo} site. However, given the distinct signal shapes at –45 ppm and –150 ppm in the ^{19}F MAS NMR spectrum of $Mo_{4/3}CT_x$, these peaks could correspond to distinct local environments, such as isolated C–F and Mo–F sites, respectively. Although we can't rigorously exclude the contribution from F in residual Al and Sc species (detected by ICP-OES) to the observed signals, the tentative assignment of the peak at –45 ppm to the covalent C–F environment is supported by the isotropic chemical shift of isolated C–F in fluorinated graphite reported at –53 ppm.[95] The broadness of the peak at –150 ppm is consistent with the distribution of Mo–F environments due to the presence of V_{Mo} sites in $Mo_{4/3}CT_x$ but contributions from conduction electrons (dipolar couplings and/or relaxation effects) cannot be ruled out. In contrast to the narrow peak at –45 ppm, the broad peak at –150 ppm largely disappears when a longer echo delay of 1 ms is used in the Hahn echo experiment (Figure S21b), showing contrasting transverse relaxation times, possibly originating from different local spin–spin and spin–electron interactions in C–F and Mo–F environments. Lastly, the formation of C–F sites in the carbon framework obtained after dissolving Mo from *m*-Mo_2CT_x in basic conditions has been reported.[96] Given that the reductive defunctionalization of –F groups in Mo_2CT_x is more facile relative to –O– and –OH groups,[52] and considering the higher amounts of –F groups in $Mo_{4/3}CT_x$, a distinct reductive defunctionalization profile can be expected for $Mo_{4/3}CT_x$ (*vide infra*).

3.3. FT Catalysis

To assess how the presence of V_{Mo} sites influences the FT performance, we tested $Mo_{4/3}CT_x$ with and without H_2 pretreatment and compared the results to those of the reference β-Mo_2C. For H_2 pretreatment, we chose 400 °C and undiluted H_2 following the previously optimized protocol for Mo_2CT_x (Figure S23).[42,97] This in situ pretreatment gave a material denoted $Mo_{4/3}CT_{x\text{–}400}$, which was subsequently exposed to an H_2:CO gas feed with a ratio of 2:1 at 330 °C under 20 bar and at a WHSV of 10.0 L $(g_{cat}\ h)^{-1}$. We allowed the first 3 h on stream for gas equilibration. Under the conditions employed, the CO conversion (X_{CO}) of $Mo_{4/3}CT_{x\text{–}400}$ was 53% at 3.7 h TOS, from which on it gradually declined, reaching 42% after 17.4 h TOS (Figure 3a, Table S6). These values correspond to rates of CO consumption (r_{CO}) of 74 $mmol_{CO}$ $(g_{cat}\ h)^{-1}$ at TOS = 3.7 h and 59 $mmol_{CO}$ $(g_{cat}\ h)^{-1}$ at TOS 17.4 h. The selectivity of $Mo_{4/3}CT_{x\text{–}400}$ did not change appreciably as X_{CO} decreased (Table S6). Specifically, the selectivity towards CO_2 is 41%, and the partial (i.e., CO_2-free) selectivity in hydrogenation products indicates that $Mo_{4/3}CT_{x\text{–}400}$ is mostly a methanation catalyst (56% CH_4 and 40% of lower C_2–C_4 alkanes). The selectivity towards $C_2{=}C_4$ olefins and C_{5+} alkanes was 1 and 3%, respectively. This is in sharp contrast to previously reported $Mo_2CT_{x\text{–}400}$, which produced, after an 8 h long activation period for an in situ reductive defunctionalization, 55% C_{5+} alkanes at r_{CO} of ca. 60 $mmol_{CO}$ $(g_{cat}\ h)^{-1}$ under comparable FT conditions (T = 330 °C, WHSV = 5.1 L $(g_{cat}\ h)^{-1}$, 25 bar).[42] The steady-state gravimetric formation rate of C_{5+} alkanes (r_{C5+}) displayed by $Mo_2CT_{x\text{–}400}$ was 15.7 $mmol_{C5+}$ $(g_{cat}\ h)^{-1}$, which exceeds that of $Mo_{4/3}CT_{x\text{–}400}$ (r_{C5+} is 0.9-1.5 $mmol_{C5+}$ $(g_{cat}\ h)^{-1}$) by about an order of magnitude.

To evaluate whether the C_{5+} selectivity can be increased, we tested unpretreated $Mo_{4/3}CT_x$ under otherwise identical FT conditions (Figure S24). In contrast to $Mo_{4/3}CT_{x\text{–}400}$ that deactivated on stream, $Mo_{4/3}CT_x$ underwent a slow in situ activation with TOS; specifically, X_{CO} increased from 41% at 3.7 h TOS to 58% at 15.6 h TOS, which corresponds to a r_{CO} of 57 and 81 $mmol_{CO}$ $(g_{cat}\ h)^{-1}$, respectively (Figure 3b). Similar to $Mo_{4/3}CT_{x\text{–}400}$, the selectivity displayed by $Mo_{4/3}CT_x$ remains largely unaffected by variations in X_{CO} (Table S7). Interestingly, $Mo_{4/3}CT_x$ exhibits a partial selectivity towards CH_4 and C_2–C_4 alkanes of 73 and 21%, respectively. That is, at comparable CO conversions, $Mo_{4/3}CT_x$ has a higher

Downloaded from pubs.acs.org/acscatal/article-pdf/16/15/14328/6529852/cs-2026-018095.pdf by LINKOPING UNIV user on 04 October 2026

https://doi.org/10.1021/acscatal.6c01809
ACS Catal. 2026, 16, 14328–14346

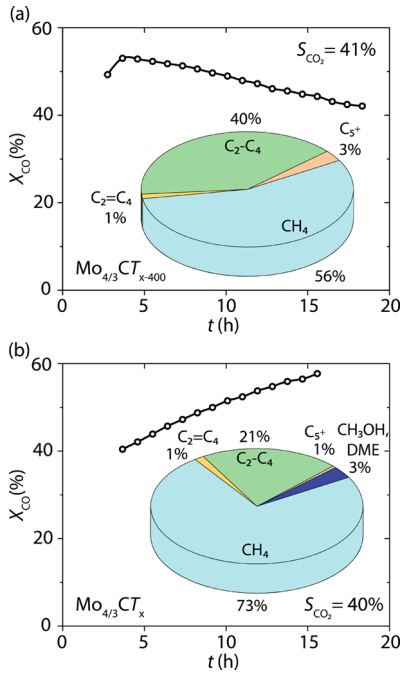

Figure 3. Conversion of CO with TOS using (a) $Mo_{4/3}CT_{x-400}$ and (b) $Mo_{4/3}CT_x$. Insets show the average CO_2-free gas-phase product distributions for $Mo_{4/3}CT_{x-400}$ and $Mo_{4/3}CT_x$, respectively, which are stable with TOS (see Tables S6 and S7 for details).

selectivity to methane and lower selectivity to C_2–C_4 alkanes than $Mo_{4/3}CT_{x-400}$. The selectivity towards C_2=C_4 olefins and C_{5+} alkanes displayed by $Mo_{4/3}CT_x$ is about 1% (r_{C5+} of 0.2 $mmol_{C5+}$ $(g_{cat}\ h)^{-1}$). In addition, $Mo_{4/3}CT_x$ produced small amounts of methanol and dimethyl ether (3%). Compared to the reference β-Mo_2C and β-$Mo_2C_{(400)}$ catalysts, which are also selective to methane (Figure S25, Table S8), the gravimetric (i.e., mass-normalized) r_{CO} of $Mo_{4/3}CT_x$ and $Mo_{4/3}CT_{x-400}$ is by a factor of ca. 20–40 higher, depending on TOS and the pretreatment conditions (see additional discussion in the SI). In the following, we apply various characterization methods to uncover structural changes in $Mo_{4/3}CT_x$ and aim to correlate such changes with variations in activity, stability, and selectivity of $Mo_{4/3}CT_x$ and $Mo_{4/3}CT_{x-400}$ under FT conditions.

3.4. Structural Evolution of $Mo_{4/3}CT_x$ under H_2 Pretreatment

To evaluate the structural changes of $Mo_{4/3}CT_x$ in reducing conditions, we performed a combined in situ XRD-PDF-XAS-MS H_2-TPR experiment. Specifically, undiluted H_2 (7 mL min^{-1}, 1 bar) was flowed through a bed of $Mo_{4/3}CT_x$ (temperature range of 50–800 °C) at a space velocity of 300 L $(g_{cat}\ h)^{-1}$. Figure 4a presents the contour plot of the evolution of the XRD patterns of $Mo_{4/3}CT_x$ during heating in an H_2 flow. Figures S26 and S27 show the detailed temperature program used and the corresponding XRD patterns, respectively. We observe that the intensity of the (002) peak of the $P6_3/mmc$ phase increases and its position shifts from 1.5° to 1.9° (λ = 0.24 Å) with increasing temperature up to 250 °C (Figure S28), indicating an increase in the degree of stacking order and a decrease in the interlayer distance from 0.9 to 0.7 nm. When increasing the temperature further, the (002) peak intensity decreases continuously, and at 400 °C, the stacking reflection is no longer visible. Furthermore, when increasing the temperature from 50 to 250 °C, the (*hk*0) peaks due to in-plane ordering shift from 3.2°, 5.4°, 6.3°, and 9.4° to 3.1°, 5.3°, 6.1°, and 9.1°, indicating an increase of the unit cell size in the in-plane direction. Thermal expansion is not expected to cause the observed shifts, as evidenced by reported in situ XRD H_2-TPR studies of $Mo_2(C,N)T_x$ that showed no appreciable changes in the (*hk*0) peaks positions up to ca. 500 °C.[50] The explanation for the observed shifts, associated with a structural transformation, will be provided using other characterization methods (*vide infra*). The temperature range of 400–575 °C is associated with the presence of peaks at 2θ = 5.6°, 6.4°, and 9.2° assigned to the nanocrystalline cubic α-MoC_{1-x} phase ($Fm\bar{3}m$ space group). The Rietveld refinement of the pattern collected at 400 °C indicates a composition of $MoC_{0.5}$, i.e., a low C atom occupancy (Figure S29 and Table S9). At 600 °C, peaks at 2θ = 5.3°, 5.8°, and 6.0° appear. These peaks are assigned to the β-Mo_2C phase (*Pbcn* space group). The appearance of these peaks indicates the transformation of H_2-treated $Mo_{4/3}CT_x$ to β-Mo_2C. Further heating to 800 °C results in the sharpening of the peaks due to β-Mo_2C, consistent with an increase in crystallinity. Rietveld refinement of the pattern collected at 800 °C suggests a stoichiometric β-Mo_2C phase (Figure S30 and Table S10).

As the X-ray diffractograms of $Mo_{4/3}CT_x$ feature broad peaks at the H_2 pretreatment temperature of the FT catalytic experiment (i.e., 400 °C), we turned to PDF analysis to obtain a direct insight into changes in local- and mid-range structure occurring during H_2 pretreatment at increasing temperatures (Figures 4b, S8, and S31). Our assignment of the interatomic pairs is based on the DFT-optimized models of a fully functionalized 2D-$Mo_{4/3}C(O)_{2/3}(F)_{4/3}$,[64] a partially defunctionalized 2D-$Mo_2CO_{0.67}$, and a fully defunctionalized 2D-Mo_2C.[42] Although the assignment of the features to specific interatomic pairs does not depend on the degree of defunctionalization or the clustering of the V_{Mo} sites (Table S1), the presence of V_{Mo} sites and the partial coverage of functional groups introduce a disorder in interatomic distances, leading to the broadening of the PDF peaks. During heating, a shoulder appears next to the feature **b** at a higher *r* value (ca. 3.2 Å); this shoulder becomes most prominent at 250 °C. At this temperature, the feature **d** shifts from 3.9 to 4.2 Å, **f** from 5.1 to 5.2 Å, and **h** from 7.8 to 7.9 Å; the increase of the interatomic distances is consistent with the expansion of the unit cell in the in-plane direction, likely due to clustering of the metal vacancy sites and the partial removal of T_x groups. The broad feature **g** of $Mo_{4/3}CT_x$ splits into two peaks at 6.0 and 6.7 Å at 250 °C, i.e., the difference in the interatomic distances of the third nearest in-plane Mo–Mo pairs and fourth nearest out-of-plane Mo–Mo pairs becomes distinguishable. The splitting suggests that the distribution of the interatomic distances caused by the presence of the metal vacancy is decreased, also consistent with the loss of ordering of the Mo vacancies. It is noted that thermal expansion alone is not expected to induce such appreciable changes, as evidenced by a reported in situ PDF H_2-TPR study of a Mo carbonitride MXene that showed an unchanging PDF pattern up to ca. 500 °C.[50] Furthermore, heating to 400 °C induces a shift of the peak maximum from 2.8 to 2.9 Å, and the shoulder in the feature **b** disappears. Additionally, features **c** and **e**, corresponding to the Mo–C atomic pairs, are dampened significantly at temperatures exceeding 250 °C, consistent with the loss of carbidic carbon (*vide infra*). The

Downloaded from pubs.acs.org/acscatal/article-pdf/16/15/14328/6529852/cs-2026-018095.pdf by LINKOPING UNIV user on 04 October 2026

https://doi.org/10.1021/acscatal.6c01809
ACS Catal. 2026, 16, 14328–14346

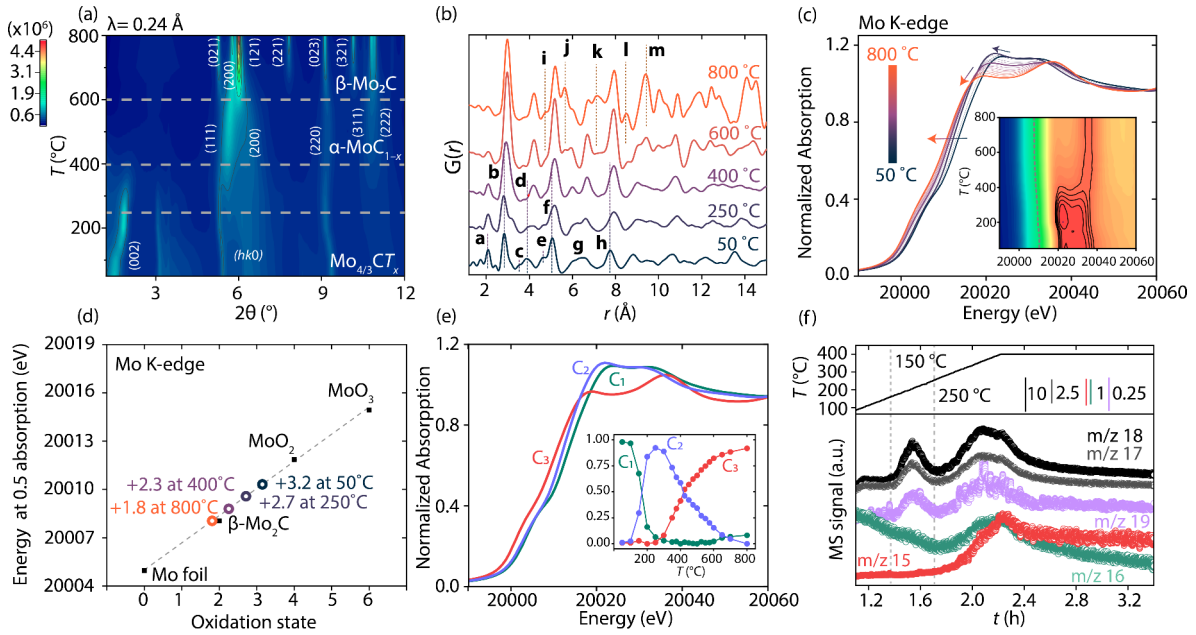

Figure 4. (a) Contour plot of the SiO_2-subtracted X-ray total scattering patterns collected at λ = 0.24 Å, (b) PDF data, (c) Mo K-edge XANES spectra (shown in the inset as a contour plot), (d) energy position for μ = 0.5 for the references Mo foil, β-Mo_2C, MoO_2, and MoO_3 and for the in situ measured $Mo_{4/3}CT_x$ at 50, 250, 400, and 800 °C, (e) XANES components obtained from an MCR-ALS analysis of the in situ H_2-TPR dataset (shown in the inset is the phase evolution of the components), and (f) off-gas analysis by mass spectrometry acquired during the in situ XAS-XRD-PDF H_2-TPR experiment using $Mo_{4/3}CT_x$ and undiluted H_2.

position of the features **d** and **f** remained unchanged at 4.2 and 5.2 Å; however, their intensity increased. The PDF patterns collected between 400 and 575 °C contain peaks at the same positions, whereby the intensity of most peaks increases with increasing temperature, indicating an increase in the local (low *r*) range order (Figure S31). The notable exceptions are features **a**, **c**, and **e**, corresponding to Mo–C pairs, which decrease with increasing temperature, explained by the continued loss of carbidic carbon. The PDF pattern collected at 400 °C was fitted with the α-MoC_{1-x} phase (specifically, fcc-$MoC_{0.681}$, see Figures S32, S34, and Table S11). This fitting verified that $Mo_{4/3}CT_x$ undergoes a phase transition at 400 °C, in agreement with XRD results, forming α-MoC_{1-x} with a coherent length of ca. 2 nm and low C atom occupancy (the PDF-fitted composition is $MoC_{0.3}$). At ca. 600 °C, a shoulder, **i**, at 4.8 Å and two new features, **j** and **k**, at 5.6 and 7.0 Å, respectively, appeared. These three features correspond to interatomic distances between Mo atoms located in the second-nearest metal layers, i.e., in the A layers of an **A**-B-C-B-**A** stacking, which is typical for β-Mo_2C, where B corresponds to carbon layers, and A and C correspond to horizontally displaced Mo layers (Figure S34).[98] Additionally, at 600 °C, features **l** and **m** appear at 8.5 and 9.4 Å, corresponding to Mo–Mo pairs residing in the third nearest metal layers (i.e., in **A** and **C** of **A**-B-C-B-A-B-**C**) of β-Mo_2C.[98,99] The fitting of the PDF pattern collected at 800 °C indicates that the formed β-Mo_2C phase (*Pbcn* space group) has a coherent length of ca. 6.8 nm and a low carbon occupancy of $Mo_2C_{0.7}$ (Figure S33 and Table S12). To summarize, the XRD and PDF results suggest that $Mo_{4/3}CT_x$ undergoes two phase transitions, i.e., α-MoC_{1-x} and β-Mo_2C form at 400 °C and 600 °C, respectively. While the 2D morphology is preserved below 400 °C, $Mo_{4/3}CT_x$ undergoes a structural transformation at 250 °C, as further elucidated by XAS.

The in situ Mo K-edge XANES profiles, collected simultaneously with the X-ray total scattering (PDF and XRD) data, are presented in Figure 4c. The inset provides the dataset as a contour plot. Figure 4d shows the calibration curve used to estimate the average oxidation states utilizing Mo foil, β-Mo_2C, MoO_2, and MoO_3 references with assigned oxidation states of 0, +2, +4, and + 6, respectively, following a previously reported method.[50] The edge energy shifts from ca. 20,010 to 20,008 eV during the H_2-TPR experiment, corresponding to a change in the average oxidation state of Mo from ca. +3.2 for $Mo_{4/3}CT_x$ at 50 °C to ca. +1.8 at 800 °C, explained by the reductive defunctionalization of T_x groups.[42,50,52,56] The spectrum at 800 °C overlaps with that of β-Mo_2C, consistent with the XRD and PDF data discussed above. The edge position of the spectra recorded at 150 and 200 °C indicates an appreciable change of ca. 0.5 eV, suggesting that the reductive defunctionalization of T_x groups occurs in this low-temperature range. Additionally, the intensity of the white line at 20,024 eV does not decrease continuously. Initially, the white line intensity increases and reaches a maximum at 250 °C, at which temperature the white line position shifts to a lower energy of 20,022 eV. As will be discussed below, these changes are attributed to clustering of V_{Mo} sites and the concomitant formation of Mo_2CT_x-like domains. Subsequently, the intensity of the white line decreases monotonically until the final temperature of 800 °C is reached (Figure 4c). An additional post-edge feature, centered around 20,033 eV, increases in intensity at temperatures above 400 °C and shifts to ca. 20,035 eV. The white line and post-edge features are observed at 20,021 and 20,035 eV for the reference Mo_2CT_x, and both are more intense, in particular, the feature at 20,021 eV (Figure S18).

A multivariate curve resolution alternating least squares (MCR-ALS) analysis of the in situ XANES dataset was performed to quantify the changes during the H_2-TPR

https://doi.org/10.1021/acscatal.6c01809
ACS Catal. 2026, 16, 14328−14346

Downloaded from pubs.acs.org/acscatal/article-pdf/16/15/14328/6529852/cs-2026-018095.pdf by LINKOPING UNIV user on 04 October 2026

experiment.[100−102] A principal component analysis (PCA) of the XANES dataset, presented in Figure S35, identifies three components, C_1, C_2, and C_3, as sufficient to reconstruct the entire dataset (Figure 4e).[103] The inset in Figure 4e displays the fractions of C_1, C_2, and C_3 as a function of temperature; the goodness of the MCR-ALS analysis of the in situ XANES dataset is provided in Table S13. While C_1 is the sole component at 50 °C, at 150 °C the spectrum can be represented by ca. 70% C_1 and 30% C_2. The latter component accounts for almost the entire spectrum at 250 °C. Component C_3 increases sharply at the expense of C_2 in the temperature range between 400 °C (60% C_2 and 40% C_3) and 600 °C (15% C_2 and 82% C_3), becoming the sole component at 800 °C. Comparing the components C_1, C_2, and C_3 with references suggests that C_1 and C_3 match the XANES profiles of $Mo_{4/3}CT_x$ and β-Mo_2C, respectively (Figure S36). It was previously reported that the XANES profiles of β-Mo_2C and α-MoC_{1-x} are similar.[104−106] Given the low-temperature onset of component C_3, we assign it to a combination of the fcc and hcp phases (α-MoC_{1-x} and β-Mo_2C). While none of our references matches the C_2 component, its increased white line intensity at 20,021 eV is reminiscent of that observed for Mo_2CT_x (Figure S36).

The Fourier transform of the EXAFS function and the fittings of $Mo_{4/3}CT_x$ after H_2 treatment at 400 and 800 °C (collected after cooling down to 50 °C) are shown in Figures S37−S39. Fitting of the EXAFS data of $Mo_{4/3}CT_{x-400}$ suggests a CN of 8(1) for the Mo–C/T_x shell at a distance of 2.11(1) Å and a CN of 4(2) for the Mo–Mo shells at 2.92(2) Å (Table 1, entry 2). The increase in the CN and interatomic distance of the Mo–Mo shell in $Mo_{4/3}CT_{x-400}$ relative to $Mo_{4/3}CT_x$ is consistent with the phase transformation to α-MoC_{1-x}, albeit the CN of 4(2) for the Mo–Mo shell is lower than the theoretical value of 12.[107] The fitted CN value for the Mo–C/T_x shell for $Mo_{4/3}CT_{x-400}$ of 8(1) is close to the theoretical value of 6 for the fcc α-MoC_{1-x} phase. The discrepancies between the identified CN values and the theoretically expected values for the cubic fcc phase are likely due to the reduced magnitude of the EXAFS function obtained. Fitting of the EXAFS data of $Mo_{4/3}CT_{x-800}$ yields a CN of 4(1) for the Mo–C shell at a distance of 2.09(1) Å and a CN of 11(1) at a distance of 2.97(1) Å (Table 1, entry 3). The fitted parameters for $Mo_{4/3}CT_{x-800}$ are very close to those of the reference β-Mo_2C (Table 1, entry 4), and their Fourier transform traces of the EXAFS function are nearly identical, corroborating the transformation to β-Mo_2C, in agreement with the XRD, PDF, and XANES data.

The off-gas from the capillary reactor during the in situ XRD-XAS-PDF H_2-TPR experiment was monitored with an MS. The spectra indicate an increase in ion currents with m/z 16 and 15 above 250 °C (Figure 4f), with a maximum at ca. 350 °C. These signals are attributed to CH_4, which forms when carbidic carbon is removed under a H_2 atmosphere, leaving V_C sites. The signals with m/z 28 and 44, ascribed to CO and CO_2, are shown in Figure S40. The temperature at which the signal at m/z 28 increases is similar to that of the signals at m/z 15 and 16, indicating that the decarburization process also leads to CO formation via the reaction of the carbidic carbon with surface oxygen. In contrast, the signal at m/z 44 progressively decreases with increasing temperature during the in situ H_2-TPR experiment and is probably not associated with the removal of carbidic carbon but rather with the release of weakly adsorbed CO_2.[108] The ion currents with m/z 18 and 17 start to appear at a lower temperature of about 150 °C (maximum of ca. 200 °C) and, at least in part, those signals are due to water formed during the reductive removal of the –O/–OH functional groups as the appearance of these ion currents correlates with changes in Mo K-edge XANES due to Mo reduction.[52] The ion current with m/z 19 is tentatively ascribed to the release of –F terminations, yet it closely resembles the water signals, indicating that the removal of –O/–OH and –F groups in $Mo_{4/3}CT_x$ may have a similar onset temperature of ca. 150 °C. The ion current at m/z 20, ascribed, accordingly, to ionized HF, was also observed and showed a profile similar to that at m/z 19 (Figure S41). The assignment of these ion currents is based on the absence of –F groups after H_2 treatment at 400 °C according to XPS analysis of the F 1s region (Figure S42). However, we note that the evolution of the profiles at m/z 17, 18, and 19 with increasing temperature is similar, which could also suggest that the m/z 19 signal is (also) due to protonated water.[97] Lastly, we note in passing that the exact conditions of H_2 treatment, such as H_2 concentration in the feed gas (e.g., 5% vs. 100%), impact the processes associated with the reductive defunctionalization of $Mo_{4/3}CT_x$. For example, under 5% H_2, the carbidic carbon is removed as CO_2 in addition to CO and CH_4 (see SI for details, including the in situ XAS-XRD-PDF 5% H_2-TPR study).

3.5. XPS and EPR Studies of Activated and Post-Reaction Catalysts

Analysis of the activated and post-reaction materials by XPS using air-tight transfers allowed us to assess changes in the electronic states of Mo and the elemental composition during FT synthesis conditions. The fitted results are presented in Table S3. The fitting of the Mo 3d XPS data indicates that $Mo_{4/3}CT_{x\text{-post-FT}}$ (i.e., post-FT-reaction catalyst without H_2 pretreatment) contains a similar amount of Mo^{+5} as fresh $Mo_{4/3}CT_x$ (24%, Figure 5a). The relative amount of the Mo^{+4} state in $Mo_{4/3}CT_{x\text{-post-FT}}$ is reduced relative to $Mo_{4/3}CT_x$ from 80 to 45%, offset by the appearance of the carbidic state, i.e., a Mo^{+2} state free of T_x groups at a BE of 228.2 eV, amounting to 31% in $Mo_{4/3}CT_{x\text{-post-FT}}$. $Mo_{4/3}CT_{x-400}$ contains 60% Mo^{+2} and 40% Mo^{+4} while $Mo_{4/3}CT_{x-400\text{-post-FT}}$ contains 61, 24, and 15% of Mo^{+2}, Mo^{+4}, and Mo^{+5} states, respectively.

Turning to the analysis of the C 1s XPS region, fresh $Mo_{4/3}CT_x$ features a peak due to carbidic carbon at 282.0 eV. Interestingly, in the activated material and in both post-FT catalysts, this peak shifts to a higher BE of 282.5 eV (Figure 5b), i.e., to a BE also observed in the reference Mo_2CT_x (Figure S19 and Table S4). Further, C–C, C=O, and COO species were present in all materials, whereas a broad, high-energy feature centered at approximately 289.9 eV, ascribed to surface-adsorbed CO_x, was identified only in the post-FT catalysts. The atomic ratio between Mo and fitted carbidic carbon, Mo : C^{carb}, is 3.2, 4.4, and 4.7 in $Mo_{4/3}CT_{x\text{-post-FT}}$, $Mo_{4/3}CT_{x-400}$, and $Mo_{4/3}CT_{x-400\text{-post-FT}}$, respectively, (Figure 5c) indicating that more than 50% of the carbidic carbon has been removed during pretreatment and FT from the XPS-probed layers, consistent with the detection of CH_4 and CO by MS and dampening of PDF features due to Mo–C pairs. These results demonstrate that both H_2 pretreatment at 400 °C and FT reaction conditions at 330 °C induce decarburization (i.e.,

https://doi.org/10.1021/acscatal.6c01809
ACS Catal. 2026, 16, 14328−14346

Downloaded from pubs.acs.org/acscatal/article-pdf/16/15/14328/6529852/cs-2026-018095.pdf by LINKOPING UNIV user on 04 October 2026

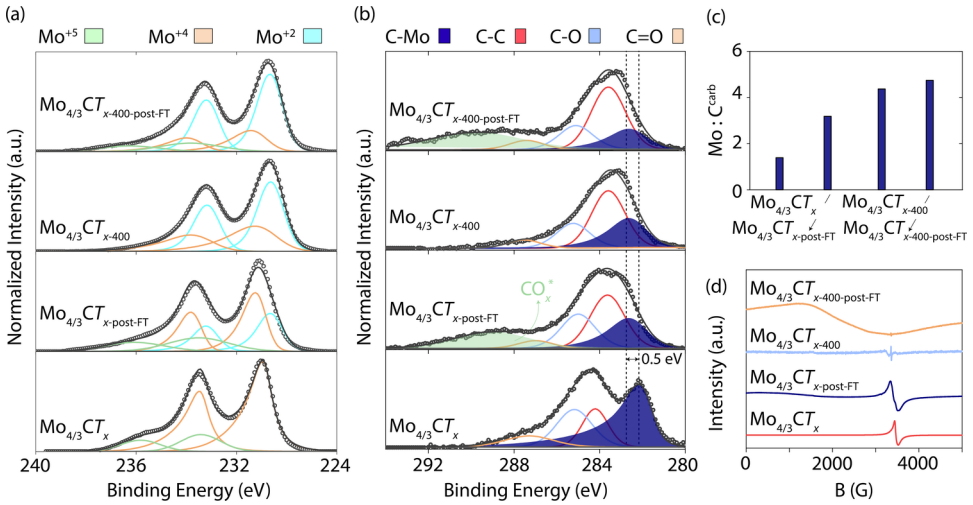

Figure 5. The fitted (a) Mo 3*d* and (b) C 1*s* XPS regions, (c) XPS-derived atomic ratio between Mo and carbidic carbon, and (d) CW-EPR spectra of $Mo_{4/3}CT_x$ and $Mo_{4/3}CT_{x\text{–}400}$ as well as post-FT catalysts $Mo_{4/3}CT_{x\text{-post-FT}}$ and $Mo_{4/3}CT_{x\text{–}400\text{-post-FT}}$ recorded at 5 K.

V_C formation) of $Mo_{4/3}CT_x$. The absence of metallic Mo in the Mo 3*d* XPS region, despite the pronounced C sub-stoichiometry, is likely to be due to the stabilization of the structure by the remaining –OH and –O– groups, as evident from the presence of oxidized Mo^{+4} and Mo^{+5} states. XPS analysis detected no fluorine in any of the activated or post-FT catalysts (Figure S42). A recent study showed that cubic $Mo_{1.3}C$ and cubic Mo_2C display Mo^{+2}, Mo^{+4} and Mo^{+5} electronic states after exposure to CO : H_2 at 2 : 1 ratio, at 250 °C and at ca. 10^{-6} bar, in line with our observations.[109]

The evolution of the atomic ratio between Mo and C during H_2 treatment and the FT reaction was also assessed in $Mo_{4/3}CT_{x\text{-post-FT}}$, $Mo_{4/3}CT_{x\text{–}400}$, and $Mo_{4/3}CT_{x\text{–}400\text{-post-FT}}$ by elemental analysis after exposure of the activated materials to ambient air (Table S14). The results indicate that the atomic Mo:C^{carb} ratios varied from 1.4 in $Mo_{4/3}CT_x$ to 1.2, 1.7, and 1.5 in $Mo_{4/3}CT_{x\text{-post-FT}}$, $Mo_{4/3}CT_{x\text{–}400}$, and $Mo_{4/3}CT_{x\text{–}400\text{-post-FT}}$, respectively. The increase of the Mo:C ratio to 1.7 in $Mo_{4/3}CT_{x\text{–}400}$ is consistent with a H_2-induced decarburization of $Mo_{4/3}CT_x$, although this integral value is appreciably lower than in the XPS-probed layers. Although the elemental analysis does not differentiate between the different types of carbon present, and it therefore underestimates the Mo:C^{carb} ratios, the near-surface layers probed with XPS are likely more carbon-depleted than the bulk, which is probed with the elemental analysis. This observation may be explained by inaccessibility of the interior MXene layers to the reactants.[50] The ratios of 1.2 and 1.5 in the post-FT catalysts are lower than those obtained with XPS, likely due to carbon deposition during FT.

The presence of Mo^{+5} or Mo^{+4} states in all XPS-studied materials motivated us to use EPR to probe for paramagnetic sites. The continuous wave (CW) EPR spectrum of Mo_2CT_x at 5 K has been reported previously and showed a signal due to Mo^{+5} sites with principal values of the **g** tensor of $g_\perp = 1.935$ and $g_\parallel = 1.890$, and a partially resolved splitting induced by the hyperfine coupling with ^{95,97}Mo nuclei (nuclear spin I = 5/2).[50,53] The signal of Mo^{+5} sites in Mo_2CT_x is detected at both 298 and 5 K (Figure S43). Fresh $Mo_{4/3}CT_x$ shows no EPR signals at 298 K (Figure S43). However, $Mo_{4/3}CT_x$ gives a signal at 5 K with the same **g** tensor as observed for Mo_2CT_x, although featuring a significantly broader linewidth and, consequently, unresolved hyperfine splitting (Figure 5d). This, together with the absence of an Mo^{+5} EPR signal at room temperature, indicates appreciably faster spin relaxation in $Mo_{4/3}CT_x$ compared to Mo_2CT_x. This is also observed through direct Hahn echo decay measurements (Figure S44). The enhanced relaxation is likely a consequence of the higher fluorine content in $Mo_{4/3}CT_x$, which is a high-gamma I = 1/2 nucleus that is hyperfine-coupled with Mo^{+5} sites.

The material $Mo_{4/3}CT_{x\text{-post-FT}}$ recovered and handled under air-free conditions exhibits a similar intensity of the Mo^{+5} signal at 5 K (Figure 5d). At the same time, its lineshape is distinct from that of $Mo_{4/3}CT_x$ due to a further broadening and change of the **g** anisotropy ($g_\perp = 1.98$ and $g_\parallel = 1.91$); these principal values of the **g** tensor are closer to the free electron values ($g_e = 2.0023$). The change of the **g** anisotropy can be induced by the coordination of a strong-field ligand, such as CO.[110] The Hahn echo decay in $Mo_{4/3}CT_{x\text{-post-FT}}$ is slower than in $Mo_{4/3}CT_x$, which can be attributed to the removal of fluorine ligands, as evidenced by XPS analysis. It should be noted that the echo-detected field-sweep spectrum of $Mo_{4/3}CT_{x\text{-post-FT}}$ (measured at 10 K), which is the equivalent of the CW spectrum in pulse mode and on which relaxation is measured, is similar to the spectra of Mo_2CT_x and $Mo_{4/3}CT_x$ (Figure S45). This suggests that only a fraction of Mo^{+5} sites that relaxes sufficiently slowly is probed in relaxation measurements, as the main species contributing to the CW spectrum of $Mo_{4/3}CT_x$ and $Mo_{4/3}CT_{x\text{-post-FT}}$ relax too quickly and therefore do not produce a spin echo. For the same reason, the signal due to isolated Mo^{+5} in the CW spectrum is invisible at room temperature. However, a new, broad, and strongly anisotropic CW signal, typical of magnetically ordered materials, appears for $Mo_{4/3}CT_{x\text{-post-FT}}$ at 298 K (Figure S43b). At 5 K, this signal is barely visible due to broadening, a typical characteristic of nanosized superparamagnetic

https://doi.org/10.1021/acscatal.6c01809
ACS Catal. 2026, 16, 14328–14346

Downloaded from pubs.acs.org/acscatcs/article-pdf/16/15/14328/6529852/cs-2026-018095.pdf by LINKOPING UNIV user on 04 October 2026

materials.[111] This observation suggests that $Mo_{4/3}CT_{x\text{-post-FT}}$ contains exchange-coupled paramagnetic states or aggregates. A notably different result is obtained for the H_2-pretreated materials. While the signal of Mo^{+5} sites is not observed for $Mo_{4/3}CT_{x-400}$, both at 298 K and 5 K (the narrow peak with g = 2.003 can be attributed to a carbon-centered defect or a V_C site), $Mo_{4/3}CT_{x-400\text{-post-FT}}$ features the broad signal due to exchange-coupled aggregates at both temperatures. The signal due to isolated Mo^{+5} sites does not reappear in $Mo_{4/3}CT_{x-400\text{-post-FT}}$, unlike in $Mo_{4/3}CT_{x\text{-post-FT}}$.

3.6. Structural Characterization of Post-Reaction Catalysts

To examine whether FT conditions induce morphological or structural differences relative to $Mo_{4/3}CT_x$ and $Mo_{4/3}CT_{x-400}$, we compared PDF patterns of the pre- and post-FT catalysts. PDF traces of the activated materials were collected in sealed capillaries without exposure to air. These data are presented in Figure 6. Relative to fresh $Mo_{4/3}CT_x$, features **a** and **c** are dampened in $Mo_{4/3}CT_{x\text{-post-FT}}$. Furthermore, the feature **b** has a shoulder at 3.2 Å, and the feature **g** is split into two peaks at 6.0 and 6.7 Å; features **d** and **f** shift from 3.9 to 4.2 Å and from 5.1 to 5.2 Å, respectively (Figure 6a). These differences make the PDF pattern of $Mo_{4/3}CT_{x\text{-post-FT}}$ distinct from that of $Mo_{4/3}CT_x$ but similar to the pattern of $Mo_{4/3}CT_x$ treated at 250 °C during the in situ H_2-TPR experiment described above, suggesting a clustering of Mo vacancies in $Mo_{4/3}CT_{x\text{-post-FT}}$. Note that the ex situ and in situ PDF traces of $Mo_{4/3}CT_{x-400}$ are similar (Figure S46), validating the comparison between the in situ and ex situ datasets. In addition, the XRD pattern of $Mo_{4/3}CT_{x\text{-post-FT}}$ is similar to the pattern of $Mo_{4/3}CT_x$ treated at 250 °C under H_2, signifying that $Mo_{4/3}CT_x$ maintains the 2D morphology under FT conditions (Figures S47a and S27). Interestingly, comparing the PDF traces of $Mo_{4/3}CT_{x-400\text{-post-FT}}$ and $Mo_{4/3}CT_{x-400}$ reveals no significant changes in the local structure (Figure 6b). Comparison between the two post-FT catalysts indicates that the features due to the Mo–C environment (**a**, **c**, and **e**) in $Mo_{4/3}CT_{x\text{-post-FT}}$ are of higher relative intensity, indicating a smaller number of V_C, in agreement with XPS results. The XRD of $Mo_{4/3}CT_{x-400\text{-post-FT}}$ reveals similar peak broadening to the pattern of $Mo_{4/3}CT_{x-400}$, suggesting that the crystallites of α-MoC_{1-x} found in the $Mo_{4/3}CT_{x-400}$ catalyst did not grow under FT conditions (Figure S47b).

The HAADF-STEM image of air-exposed $Mo_{4/3}CT_{x\text{-post-FT}}$ is presented in Figure S48 with the corresponding FFT image shown as an inset. The spotted rings of the FFT pattern indicate a lower degree of crystallinity compared to fresh $Mo_{4/3}CT_x$. The rings in the FFT image correspond to the *hk*0 reflections due to in-plane ordering. The 1D SAED profile and its comparison to the air-tight XRD pattern are provided in Figure S47. Different relative intensities are observed between the SAED and the XRD profiles. This is likely because single flakes are measured to obtain SAED patterns that display preferential orientation, whereas flakes in powder XRD are randomly oriented. The HAADF image of air-exposed $Mo_{4/3}CT_{x\text{-post-FT}}$ shows the presence of voids with an average diameter of 1.4 ± 0.3 nm (Figure S49), which is approximately 50% larger than the voids presumably formed due to the beam damage and clustering of the V_{Mo} sites in fresh $Mo_{4/3}CT_x$ discussed above. This result is consistent with V_{Mo} clustering under FT conditions.

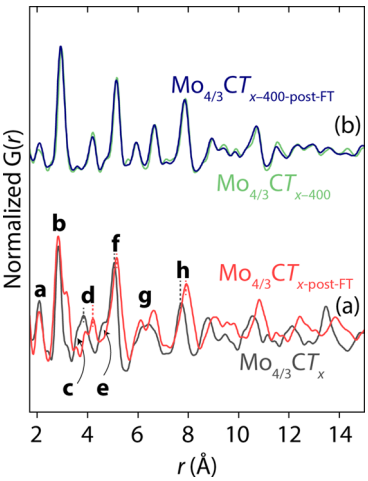

Figure 6. Ex situ PDF profiles comparing (a) $Mo_{4/3}CT_x$ and $Mo_{4/3}CT_{x\text{-post-FT}}$, (b) $Mo_{4/3}CT_{x-400}$ and $Mo_{4/3}CT_{x-400\text{-post-FT}}$. Except for $Mo_{4/3}CT_x$, all materials were handled in air-tight conditions.

4. DISCUSSION

4.1. H_2-Induced T_x Defunctionalization, V_{Mo} Clustering, and V_C Formation

Our in situ H_2-TPR experiment reveals a notable change in the Mo K-edge energy between 150 and 200 °C, which implies a shift in the electronic environment of Mo sites, consistent with their reduction. At the same time, the effluent gas analysis by MS identifies H_2O and, likely, HF (linked to species with *m*/*z* 17, 18, and 19), confirming the release of the T_x groups at temperatures >150 °C. At 250 °C, the clustering of the initially ordered V_{Mo} sites and the formation of Mo_2CT_x-like domains are evident. Indications of V_{Mo} clustering include a shift of the (*hk*0) peaks towards lower angles during heating to 250 °C, associated with an expansion of the unit cell in the in-plane direction. The unit cell expansion is also observed in the PDF pattern of $Mo_{4/3}CT_{x-250}$ (in situ dataset), which reveals an increase in the interatomic distances of features **d**, **f**, and **h**. Furthermore, Mo–Mo distances at 2.8 and 3.2 Å (a shoulder to feature **b**) are observed, with the in-plane distance (linked to the higher intensity peak) being the shorter one. A similar peak splitting by 0.5 Å is also observed between the nearest in- and out-of-plane distances in Mo_2CT_x (2.7 and 3.3 Å). The feature **g** in $Mo_{4/3}CT_x$ is broad due to the distribution of interatomic distances for pairs residing on either side of a Mo vacancy; this feature splits into two well-defined peaks at 6.0 and 6.7 Å at 250 °C. Also in line with V_{Mo} clustering, the Mo K-edge XANES of $Mo_{4/3}CT_x$ displays an increase in the white line intensity upon heating to 250 °C. This change is instructive because both the reductive defunctionalization of the T_x groups (onset at ca. 150 °C) and the removal of carbidic carbon as CH_4 and CO (onset at ca. 250 °C) reduce Mo sites in $Mo_{4/3}CT_x$ and are therefore expected to decrease the white line intensity.[112] In comparison, this decrease has been observed for Mo_2CT_x and $Mo_2(C,N)T_x$ during H_2 treatment.[50,52] The increase in the white line intensity of $Mo_{4/3}CT_x$ during H_2 treatment to 250 °C could therefore be due to a *p*-*d* rehybridization upon the clustering of the initially-ordered V_{Mo} sites, such that the local structure of the Mo atoms in $Mo_{4/3}CT_{x-250}$ resembles that of Mo_2CT_x

https://doi.org/10.1021/acscatal.6c01809
ACS Catal. 2026, 16, 14328−14346

Downloaded from pubs.acs.org/acscatcs/article-pdf/16/15/14328/6529452/cs-2026-018095.pdf by LINKOPING UNIV user on 04 October 2026

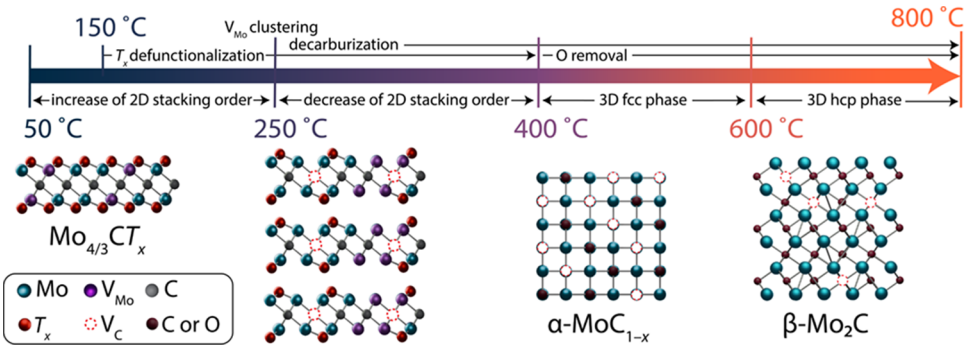

Figure 7. Schematic representation of the key structural changes occurring during H_2 treatment of $Mo_{4/3}CT_x$.

(i.e., it forms Mo_2CT_x-like domains).[113] Additionally, the position of the white line in $Mo_{4/3}CT_{x-250}$ is 20,022 eV, which is closer to the 20,021 eV white line of Mo_2CT_x than the 20,024 eV white line of $Mo_{4/3}$ CT_x. The release of carbidic carbon as CH_4 and CO (detected in the effluent gas due to signals at m/z 16 and 15, and 28, respectively) has an onset temperature of approximately 250 °C, suggesting that the loss of carbidic carbon occurs from a partially functionalized $Mo_{4/3}CT_x$. As the onset of decarburization follows the clustering of the initially ordered V_{Mo} sites, it is conceivable that decarburization is also driven by this clustering. The formation of V_C sites has been reported for Mo_2CT_x and $Mo_2(C,N)T_x$, albeit at a significantly higher temperature of ca. 450 °C, indicating that the presence of V_{Mo} sites destabilizes carbidic carbon under H_2 atmosphere.[42,50]

4.2. Crystallinity and Phase Transitions

The XRD data collected during the H_2-TPR experiment show an increase in the (002) peak up to 250 °C, followed by a gradual decrease and disappearance at 400 °C. These results suggest that the initial heating up to 250 °C increases the limited stacking order of as-prepared $Mo_{4/3}CT_x$, whereas further heating (i.e., >250 °C) disrupts the stacking order of the nanosheets. Both in situ XRD and PDF datasets verify the transformation of $Mo_{4/3}CT_x$ to a nanocrystalline 3D cubic α-MoC_{1-x} phase at 400 °C and to a 3D orthorhombic β-Mo_2C phase at 600 °C. Previous studies of the structural evolution of Mo_2CT_x and $Mo_2(C,N)T_x$ with increasing temperature under H_2 identified a phase transformation to a 3D orthorhombic β-Mo_2C and β-$Mo_2(C,N)$ phases, respectively, between 500 and 600 °C; however, no intermediate fcc phase was formed,[42,50,52,56] in a sharp contrast to the structural evolution of $Mo_{4/3}CT_x$ studied here. The XANES spectrum of $Mo_{4/3}CT_{x-400}$ can be represented, based on the MCR-ALS analysis, by a combination containing 40% of the component C_3 (a carbidic component) and 60% of the partially functionalized component C_2 (represented by $Mo_{4/3}CT_{x-250}$). This result suggests that the complete reductive defunctionalization of delaminated $Mo_{4/3}CT_x$ either does not take place before its transformation into the 3D phase or occurs concurrently with it. This is in contrast to the reductive defunctionalization of multilayered Mo_2CT_x, which gives T_x free 2D-Mo_2C_{1-x} at 500 °C without transitioning to the 3D structure.[42,56] Such a difference may be due to the higher amount of V_C sites in the H_2-treated $Mo_{4/3}CT_x$, relative to Mo_2CT_x; note that the higher O affinity of carbon-deficient 3D molybdenum carbides has been previously reported.[46] Figure 7 summarizes these observations.

4.3. Evolution of $Mo_{4/3}CT_x$ under FT Conditions

The XRD and PDF patterns of $Mo_{4/3}CT_{x\text{-post-FT}}$ are similar to those of $Mo_{4/3}CT_{x-250}$ of the in situ H_2-TPR experiment, suggesting that FT reaction conditions (1CO : $2H_2$, 20 bar, 330 °C) also induce the clustering of V_{Mo} sites. Thus, the ordering of the V_{Mo} sites is lost under both FT conditions and H_2 at 250 °C. The ex situ PDF analysis of pristine $Mo_{4/3}CT_{x-400}$ and both post-FT catalysts demonstrates a decrease in the amplitudes of the features **a**, **c**, and **e** ascribed to Mo–C pairs and therefore indicates that all three materials have lost carbidic carbon. This is consistent with the air-tight ex situ XPS analysis of $Mo_{4/3}$ CT_{x-400} and both post-FT catalysts, which show a significantly increased $Mo:C^{carb}$ ratio, corroborating the loss of carbidic carbon in these materials. Overall, the clustering of V_{Mo} sites and the formation of V_C sites in $Mo_{4/3}CT_x$ proceed both under high-temperature FT conditions (i.e., under CO atmosphere) and H_2 pretreatment.

The air-tight Mo 3*d* XPS analysis suggests that $Mo_{4/3}$ CT_{x-400} contains Mo^{+2} and Mo^{+4} states, corresponding to a partial coverage of T_x groups, in contrast to $Mo_{4/3}CT_x$, which contains Mo^{+4} and Mo^{+5} states and is fully T_x-covered. Both post-FT catalysts contain a mixture of Mo^{+2}, Mo^{+4}, and Mo^{+5} states, consistent with the reduction of $Mo_{4/3}CT_x$ and oxidation of $Mo_{4/3}CT_{x-400}$ under reaction conditions, and are therefore partially defunctionalized.

Mo_2C-based catalysts rely on carbidic Mo^{+2} as active sites.[24,42,114] Notably, $Mo_{4/3}CT_x$ and $Mo_{4/3}CT_{x-400}$ reveal divergent trends of CO conversion and the CO conversion rate with time on stream, i.e., $Mo_{4/3}CT_x$ activates while $Mo_{4/3}$ CT_{x-400} deactivates with TOS. Specifically, the highest r_{CO} of 74 $mmol_{CO}$ $(g_{cat}\ h)^{-1}$ was obtained for $Mo_{4/3}CT_{x-400}$ at TOS = 3.7 h, while $Mo_{4/3}CT_x$ yielded a similar r_{CO} of 81 $mmol_{CO}$ $(g_{cat}\ h)^{-1}$ after ca. 15.6 h on stream. The increasing CO conversion with TOS displayed by $Mo_{4/3}CT_x$ correlates with the reductive defunctionalization of the T_x groups under FT conditions, as seen from the appearance of the Mo^{+2} (31%) state at the expense of the Mo^{+4} state, which correlates with the XPS-based average Mo oxidation state of +4.2 before the FT reaction and +3.6 after 15.6 h of TOS. The decreasing CO conversion with TOS displayed by $Mo_{4/3}CT_{x-400}$ correlates with the appearance of the Mo^{+5} state at the expense of the Mo^{+4} state under FT conditions,[109] corresponding to only a slight increase of the XPS-based average Mo oxidation state from +2.8 in $Mo_{4/3}CT_{x-400}$ before the catalytic test to +2.9 after 17.4 h of TOS. Irrespective of the starting state, the $Mo_{4/3}CT_x$-derived catalysts converge under FT conditions to a mixture of Mo^{+2}, Mo^{+4}, and Mo^{+5} states. The diverging stability trends between $Mo_{4/3}CT_x$ and $Mo_{4/3}CT_{x-400}$ are likely due to the lower oxophilicity of

https://doi.org/10.1021/acscatal.6c01809
ACS Catal. 2026, 16, 14328−14346

Downloaded from pubs.acs.org/acscatcs/article-pdf/16/15/14328/6529852/cs-2026-018095.pdf by LINKOPING UNIV user on 04 October 2026

$Mo_{4/3}CT_x$ under FT conditions relative to the oxophilicity of the strongly carbon-deficient 3D α-MoC_{1-x} phase. The FT activity of various molybdenum carbide catalysts and reported Fe, Co, and Ru catalysts is provided in Table S16. Overall, the activity and selectivity of the $Mo_{4/3}CT_x$–based catalysts toward higher alkanes are comparable to that of high-surface-area molybdenum carbide nanoparticles (ca. 106 m^2 g^{-1}) at similar testing conditions.[40] Relative to promoted Fe- and Co-based SiO_2-supported catalysts, the $Mo_{4/3}CT_x$–based catalysts favor methane and short-chain C_2–C_4 alkanes rather than C_{5+} hydrocarbons and also result in high selectivity towards CO_2.[115]

4.4. Pretreatment-Dependent Active Sites

While $Mo_{4/3}CT_{x\text{-post-FT}}$ and $Mo_{4/3}CT_{x\text{–400-post-FT}}$ are both partially oxidized, these materials display distinct rates of CO conversion, i.e., 81 $mmol_{CO}$ $(g_{cat}\ h)^{-1}$ at TOS = 15.6 h and 59 $mmol_{CO}$ $(g_{cat}\ h)^{-1}$ at TOS = 17.4 h, respectively. Moreover, $Mo_{4/3}CT_{x\text{-post-FT}}$ displays a higher r_{CO} with a lower (32%) relative amount of the Mo^{+2} state (according to XPS) compared to a higher relative amount (61%) of the Mo^{+2} state in $Mo_{4/3}CT_{x\text{–400-post-FT}}$, which, at the same time, displays a lower r_{CO}. As described above, the observed differences in catalytic activity are likely due to the distinct local structure of the active sites present in $Mo_{4/3}CT_{x\text{-post-FT}}$ (2D morphology after V_{Mo} clustering and V_C formation) and $Mo_{4/3}CT_{x\text{–400-post-FT}}$ (V_C-rich 3D fcc phase).

Furthermore, comparing the reaction rates of activated $Mo_{4/3}CT_x$ and Mo_2CT_x indicates either the potential presence of oxygen in V_C sites in $Mo_{4/3}CT_x$ or a higher intrinsic activity of Mo^{+2} sites in $Mo_{4/3}CT_x$. Specifically, a r_{CO} of ca. 60–80 $mmol_{CO}$ $(g_{cat}\ h)^{-1}$ displayed by $Mo_{4/3}CT_x$-derived catalysts is similar to ca. 60 $mmol_{CO}$ $(g_{cat}\ h)^{-1}$ displayed by $Mo_2CT_{x\text{–400}}$ and $Mo_2CT_{x\text{–500}}$ under the steady-state conditions and with the T_x-free (i.e., with only Mo^{+2}) surface sites.[42] Note that $Mo_2CT_{x\text{–400}}$ at TOS = 3.8 h, i.e., prior to reaching a steady state, and with T_x groups present, showed a ca. 6 times lower r_{CO} of 11 $mmol_{CO}$ $(g_{cat}\ h)^{-1}$.[42] The gravimetric rates displayed by in situ activated $Mo_{4/3}CT_x$ catalyst is therefore similar to the reported rates of T_x-free 2D-Mo_2C and 2D-Mo_2C_{1-x}.[42]

We have previously reported that the Mo : C^{carb} stoichiometry assessed by XPS correlates with FT selectivity for Mo_2CT_x. Specifically, a substoichiometric Mo : C^{carb} ratio of 3 correlated with methanation selectivity of $Mo_2CT_{x\text{–500}}$ in FT conditions, while a Mo : C^{carb} ratio of ca. 1.9 ($Mo_2CT_{x\text{–400}}$) correlated with selectivity to kerosine-range alkanes.[42] For Mo_2CT_x, V_C sites formed only during H_2 pretreatment above 450 °C and did not form under FT conditions (1 CO : 2 H_2, 330 °C, 25 bar). In contrast, the Mo : C^{carb} ratio in $Mo_{4/3}CT_{x\text{-post-FT}}$ is ca. 3, which is higher than the initial ratio of 1.4 in fresh $Mo_{4/3}CT_x$. Furthermore, the similar Mo:C^{carb} ratio of 4.4 and 4.7 in $Mo_{4/3}CT_{x\text{–400}}$ and $Mo_{4/3}CT_{x\text{–400-post-FT}}$, respectively, suggests that V_C sites formed during H_2 pretreatment are not replenished under the FT conditions used. These results underscore that the presence of V_{Mo} sites in $Mo_{4/3}CT_x$ decreases the stability of lattice carbon, leading to V_C formation at lower temperatures both under H_2 treatment and FT conditions. $Mo_{4/3}CT_x$ and $Mo_{4/3}CT_{x\text{–400}}$ produce CH_4 with a partial selectivity of 73 and 56%, which correlates with the presence of V_C sites. A rapid diffusion of CH_x* fragments (i.e., surface mobility) is an essential feature of an effective FT catalyst that enables two CH_x* fragments to form a C–C bond at a chain growth site.[116] The presence of V_{Mo} in $Mo_{4/3}CT_x$ is expected to increase the diffusion barriers of CH_x* species and thereby hamper the chain growth.[117] Given the presence of clustered V_{Mo} sites in $Mo_{4/3}CT_x$ under FT conditions, the diffusivity of CH_x* species on its surface is expected to be lower than in 2D-Mo_2C without the V_{Mo} sites, and also lower than in $Mo_{4/3}CT_{x\text{–400}}$ with its nanocrystalline α-MoC_{1-x} phase, thereby reducing selectivity to C_2–C_4 products, as is experimentally observed. In addition, FeC_x-based catalysts have been reported to catalyze FT via a dynamic process involving C^{carb}.[118] As C^{carb} is largely unavailable in $Mo_{4/3}CT_x$ and $Mo_{4/3}CT_{x\text{–400}}$ due to facile V_C formation, the mechanism involving C^{carb} is disfavored for the catalysts of this work. Figure 8 summarizes catalytic results.

5. CONCLUSIONS

In this work, we studied the reductive defunctionalization and FT performance of the *i*-MXene $Mo_{4/3}CT_x$ that contains ordered metal vacancies in its as-synthesized state. We found that $Mo_{4/3}CT_x$-based catalysts are active and yield CO consumption rates of about 60–80 $mmol_{CO}$ $(g_{cat}\ h)^{-1}$ but are poorly selective to liquid alkanes, producing CH_4 primarily. Their stability with TOS varies depending on the pretreatment (H_2 pretreatment or no pretreatment). The presence of Mo vacancies in $Mo_{4/3}CT_x$ destabilizes carbidic carbon under reductive conditions as compared to the reference MXene Mo_2CT_x that does not contain Mo vacancies. Under H_2 treatment conditions, the partial defunctionalization of the T_x groups precedes the clustering of Mo vacancies and the formation of carbon vacancies. The carbon vacancies formed are particularly abundant in the exterior layers and are not replenished under FT conditions. The high CO consumption rates of $Mo_{4/3}CT_x$ suggest that the oxygen present

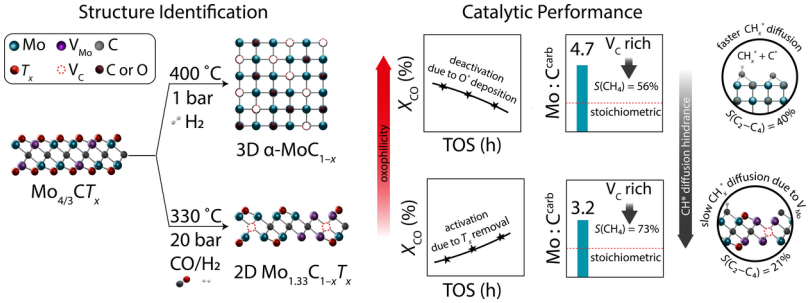

Figure 8. Schematic representation of the structure-activity relationships in $Mo_{4/3}CT_x$ in the FT reaction. $Mo_{4/3}C$ and $Mo_{1.33}C$ notations correspond to ordered and random/clustered distribution of Mo vacancies in the lattice, respectively.

https://doi.org/10.1021/acscatal.6c01809
ACS Catal. 2026, 16, 14328–14346

Downloaded from pubs.acs.org/acscatal/article-pdf/16/15/14328/6529852/cs-2026-018095.pdf by LINKOPING UNIV user on 04 October 2026

under operating conditions does not block the active sites. The carbon-deficient $Mo_{4/3}CT_x$ displays a high affinity towards oxygen and therefore cannot be fully reduced without the concomitant transformation into a 3D fcc MoC_{1-x} phase. Once formed, this phase leads to a catalyst deactivation in FT conditions. Overall, Mo vacancies render 2D molybdenum carbides more prone to form carbon vacancies, which in turn correlates with a lower reducibility for the partially functionalized Mo carbides and a higher selectivity towards methanation.

■ ASSOCIATED CONTENT

Supporting Information

The Supporting Information is available free of charge at https://pubs.acs.org/doi/10.1021/acscatal.6c01809.

Experimental procedures, characterization, additional results, fittings of the experimental data, and comparison of the catalytic results in this work with literature reports (PDF)

■ AUTHOR INFORMATION

Corresponding Author

Alexey Fedorov – *Department of Mechanical and Process Engineering, ETH Zürich, Zürich CH-8092, Switzerland*; orcid.org/0000-0001-9814-6726; Email: fedoroal@ethz.ch

Authors

Evgenia Kountoupi – *Department of Mechanical and Process Engineering, ETH Zürich, Zürich CH-8092, Switzerland*; orcid.org/0000-0002-7766-6172

Yevkeni Wisse – *Unité de Catalyse et Chimie du Solide, Université Lille, CNRS, Centrale Lille, Université d'Artois, UMR 8181, Arras 62000, France*

Mikhail Agrachev – *Department of Chemistry and Applied Biosciences, ETH Zürich, Zürich CH-8093, Switzerland*; orcid.org/0000-0001-7915-400X

Faidra Amargianou – *Helmholtz-Zentrum Berlin für Materialien und Energie, Berlin 12489, Germany*

Joseph Halim – *Department of Physics, Chemistry and Biology, Linköping University, Linköping SE-58183, Sweden*; orcid.org/0000-0002-7502-1215

Diana Piankova – *Department of Mechanical and Process Engineering, ETH Zürich, Zürich CH-8092, Switzerland*; orcid.org/0000-0002-3098-6822

Leiqiang Qin – *Department of Physics, Chemistry and Biology, Linköping University, Linköping SE-58183, Sweden*; orcid.org/0000-0002-7047-0927

Pierre Florian – *CNRS, CEMHTI UPR3079, Université d'Orléans, Orléans 45071, France*; orcid.org/0000-0003-4306-0815

Paula M. Abdala – *Department of Mechanical and Process Engineering, ETH Zürich, Zürich CH-8092, Switzerland*; orcid.org/0000-0002-2011-1707

Gunnar Jeschke – *Department of Chemistry and Applied Biosciences, ETH Zürich, Zürich CH-8093, Switzerland*; orcid.org/0000-0001-6853-8585

Tristan Petit – *Helmholtz-Zentrum Berlin für Materialien und Energie, Berlin 12489, Germany*; orcid.org/0000-0002-6504-072X

Vitaly V. Ordomsky – *Unité de Catalyse et Chimie du Solide, Université Lille, CNRS, Centrale Lille, Université d'Artois, UMR 8181, Arras 62000, France*; orcid.org/0000-0002-4814-5052

Christoph R. Müller – *Department of Mechanical and Process Engineering, ETH Zürich, Zürich CH-8092, Switzerland*; orcid.org/0000-0003-2234-6902

Johanna Rosen – *Department of Physics, Chemistry and Biology, Linköping University, Linköping SE-58183, Sweden*; orcid.org/0000-0002-5173-6726

Complete contact information is available at: https://pubs.acs.org/doi/10.1021/acscatal.6c01809

Author Contributions

E.K. and A.F. conceived the research project, designed the experiments, and wrote the paper with contributions from all authors. Y.W. performed the catalytic tests, and V.V.O. supervised them. M.A. performed EPR measurements that M.A. and G.J. analyzed. F.A. performed STXM measurements, and T.P. supervised them. J.H. and L.Q. synthesized $Mo_{4/3}CT_x$ and delaminated Mo_2CT_x materials, which J.R. supervised. D.P. performed microscopy studies and analyzed the data. P.F. performed MAS NMR measurements. All other experiments were performed by E.K., who also analyzed the data. P.M.A. provided feedback on the XRD, PDF, and XAS data analysis. C.R.M. provided resources for this work and participated in discussions. All authors gave their approval to the final version of the manuscript.

Notes

The authors declare no competing financial interest.

■ ACKNOWLEDGMENTS

ETH Zürich supported this work through a doctoral fellowship to E.K. (ETH-40 19-2). D.P. acknowledges the SNSF for financial support through the grant TMPFP2_224646. Y.W. and V.V.O. acknowledge the financial support from the French National Research Agency (DEZECO, ANR-22-CE05-0005). STXM investigations received funding from the European Research Council (ERC) under the European Union's Horizon 2020 research and innovation program (Grant Agreement No. 947852). The authors thank the Helmholtz-Zentrum Berlin für Materialien und Energie for the allocation of synchrotron radiation beamtime and Tianxiao Sun and Markus Weigand for experimental support. J.R. acknowledges support from the Knut and Alice Wallenberg (KAW) foundation for a Scholar Grant (2023.0250). We are grateful to the Scientific Centre for Optical and Electron Microscopy (ScopeM, ETH Zürich) for providing access to electron microscopy facilities. We thank Prof. Dr. Victor Mougel and Dr. Robin Dürr (both ETH Zürich) for granting us access to the XPS instrumentation and for its maintenance, respectively. We thank Dr. Agnieszka Kierzkowska for the in-house ICP-OES analysis. This publication was created as a part of NCCR Catalysis (grant number 180544), a National Centre of Competence in Research funded by the Swiss National Science Foundation.

Downloaded from pubs.acs.org/acscatal/article-pdf/16/15/14328/6529452/cs-2026-018095.pdf by LINKOPING UNIV user on 04 October 2026

The Swiss Norwegian Beamlines (SNBL) at ESRF are acknowledged for providing beamtime under proposal A31-1-194. The BM31 setup at SNBL was funded by the Swiss National Science Foundation (grant 20602118629) and the Research Council of Norway (grant 296087).

REFERENCES

(1) Fischer, F.; Tropsch, H. Über die Direkte Synthese von Erdöl-Kohlenwasserstoffen bei Gewöhnlichem Druck. (Zweite Mitteilung). *Ber. Dtsch. Chem. Ges.* **1926**, *59*, 832–836.
(2) Rommens, K. T.; Saeys, M. Molecular Views on Fischer–Tropsch Synthesis. *Chem. Rev.* **2023**, *123*, 5798–5858.
(3) Weststrate, C. J.; Sharma, D.; Garcia Rodriguez, D.; Gleeson, M. A.; Fredriksson, H. O. A.; Niemantsverdriet, J. W. Mechanistic Insight into Carbon-Carbon Bond Formation on Cobalt under Simulated Fischer-Tropsch Synthesis Conditions. *Nat. Commun.* **2020**, *11*, No. 750.
(4) Weststrate, C. J.; van Helden, P.; Niemantsverdriet, J. W. Reflections on the Fischer-Tropsch Synthesis: Mechanistic Issues from a Surface Science Perspective. *Catal. Today* **2016**, *275*, 100–110.
(5) Singh, H.; Li, C.; Cheng, P.; Wang, X.; Liu, Q. A critical review of technologies, costs, and projects for production of carbon-neutral liquid e-fuels from hydrogen and captured CO_2. *Energy Adv.* **2022**, *1*, 580–605.
(6) Cuéllar-Franca, R.; García-Gutiérrez, P.; Dimitriou, I.; Elder, R. H.; Allen, R. W. K.; Azapagic, A. Utilising carbon dioxide for transport fuels: The economic and environmental sustainability of different Fischer-Tropsch process designs. *Appl. Energy* **2019**, *253*, No. 113560.
(7) Dry, M. E. The Fischer–Tropsch Process: 1950–2000. *Catal. Today* **2002**, *71*, 227–241.
(8) Visconti, C. G.; Tronconi, E.; Groppi, G.; Lietti, L.; Iovane, M.; Rossini, S.; Zennaro, R. Monolithic catalysts with high thermal conductivity for the Fischer–Tropsch synthesis in tubular reactors. *Chem. Eng. J.* **2011**, *171*, 1294–1307.
(9) Visconti, C. G.; Tronconi, E.; Lietti, L.; Zennaro, R.; Forzatti, P. Development of a complete kinetic model for the Fischer–Tropsch synthesis over Co/Al_2O_3 catalysts. *Chem. Eng. Sci.* **2007**, *62*, 5338–5343.
(10) Schmider, D.; Maier, L.; Deutschmann, O. Reaction Kinetics of CO and CO_2 Methanation over Nickel. *Ind. Eng. Chem. Res.* **2021**, *60*, 5792–5805.
(11) Rofer-DePoorter, C. K. A Comprehensive Mechanism for the Fischer-Tropsch Synthesis. *Chem. Rev.* **1981**, *81*, 447–474.
(12) van Santen, R. A.; Markvoort, A. J.; Filot, I. A. W.; Ghouri, M. M.; Hensen, E. J. M. Mechanism and microkinetics of the Fischer–Tropsch reaction. *Phys. Chem. Chem. Phys.* **2013**, *15*, 17038–17063.
(13) Kummer, J. T.; DeWitt, T. W.; Emmett, P. H. Some Mechanism Studies on the Fischer-Tropsch Synthesis Using C^{14}. *J. Am. Chem. Soc.* **1948**, *70*, 3632–3643.
(14) Niemantsverdriet, J. W.; Van der Kraan, A. M.; Van Dijk, W. L.; Van der Baan, H. S. Behavior of Metallic Iron Catalysts During Fischer-Tropsch Synthesis Studied with Mössbauer Spectroscopy, X-ray Diffraction, Carbon Content Determination, and Reaction Kinetic Measurements. *J. Phys. Chem.* **1980**, *84*, 3363–3370.
(15) Xiang, Y.; Kovarik, L.; Kruse, N. Rate and Selectivity Hysteresis During the Carbon Monoxide Hydrogenation over Promoted Co/MnO_x Catalysts. *Nat. Commun.* **2019**, *10*, No. 3953.
(16) de Smit, E.; Cinquini, F.; Beale, A. M.; Safonova, O. V.; van Beek, W.; Sautet, P.; Weckhuysen, B. M. Stability and Reactivity of ϵ–χ–θ Iron Carbide Catalyst Phases in Fischer–Tropsch Synthesis: Controlling μ_C. *J. Am. Chem. Soc.* **2010**, *132*, 14928–14941.
(17) Amelse, J. A.; Butt, J. B.; Schwartz, L. H. Carburization of Supported Iron Synthesis Catalysts. *J. Phys. Chem.* **1978**, *82*, 558–563.
(18) Raupp, G. B.; Delgass, W. N. Mössbauer Investigation of Supported Fe Catalysts: III. In Situ Kinetics and Spectroscopy During Fischer-Tropsch Synthesis. *J. Catal.* **1979**, *58*, 361–369.
(19) Chang, Q.; Zhang, C.; Liu, C.; Wei, Y.; Cheruvathur, A. V.; Dugulan, A. I.; Niemantsverdriet, J. W.; Liu, X.; He, Y.; Qing, M.; et al. Relationship Between Iron Carbide Phases (ε-Fe_2C, Fe_7C_3, and χ-Fe_5C_2) and Catalytic Performances of Fe/SiO_2 Fischer–Tropsch Catalysts. *ACS Catal.* **2018**, *8*, 3304–3316.
(20) Gracia, J. M.; Prinsloo, F. F.; Niemantsverdriet, J. W. Mars-van Krevelen-like Mechanism of CO Hydrogenation on an Iron Carbide Surface. *Catal. Lett.* **2009**, *133*, 257–261.
(21) Huo, C.-F.; Li, Y.-W.; Wang, J.; Jiao, H. Insight into CH_4 Formation in Iron-Catalyzed Fischer–Tropsch Synthesis. *J. Am. Chem. Soc.* **2009**, *131*, 14713–14721.
(22) Ordomsky, V. V.; Legras, B.; Cheng, K.; Paul, S.; Khodakov, A. Y. The Role of Carbon Atoms of Supported Iron Carbides in Fischer–Tropsch Synthesis. *Catal. Sci. Technol.* **2015**, *5*, 1433–1437.
(23) Leclercq, L.; Imura, K.; Yoshida, S.; Barbee, T.; Boudart, M. Synthesis of New Catalytic Materials: Metal Carbides of the Group VI B Elements. In: *Studies in Surface Science and Catalysis*, Delmon, B.; Grange, P.; Jacobs, P.; Poncelet, G., Vol *3*, *Elsevier, 1979*; pp 627–639.
(24) Ranhotra, G. S.; Bell, A. T.; Reimer, J. A. Catalysis over Molybdenum Carbides and Nitrides: II. Studies of CO Hydrogenation and C_2H_6 Hydrogenolysis. *J. Catal.* **1987**, *108*, 40–49.
(25) Kim, H.-G.; Lee, K. H.; Lee, J. S. Carbon Monoxide Hydrogenation over Molybdenum Carbide Catalysts. *Res. Chem. Intermed.* **2000**, *26*, 427–443.
(26) Kojima, I.; Miyazaki, E. Catalysis by Transition Metal Carbides: V. Kinetic Measurements of Hydrogenation of CO over TaC, TiC, and Mo_2C catalysts. *J. Catal.* **1984**, *89*, 168–171.
(27) Sullivan, M. M.; Held, J. T.; Bhan, A. Structure and Site Evolution of Molybdenum Carbide Catalysts upon Exposure to Oxygen. *J. Catal.* **2015**, *326*, 82–91.
(28) Xiong, K.; Yu, W.; Chen, J. G. Selective Deoxygenation of Aldehydes and Alcohols on Molybdenum Carbide (Mo_2C) surfaces. *Appl. Surf. Sci.* **2014**, *323*, 88–95.
(29) Nørskov, J. K.; Abild-Pedersen, F.; Studt, F.; Bligaard, T. Density functional theory in surface chemistry and catalysis. *PNAS* **2011**, *108*, 937–943.
(30) Kayode, G. O.; Montemore, M. M. Factors controlling oxophilicity and carbophilicity of transition metals and main group metals. *J. Mater. Chem. A* **2021**, *9*, 22325–22333.
(31) Chen, C.-J.; Bhan, A. Mo_2C Modification by CO_2, H_2O, and O_2: Effects of Oxygen Content and Oxygen Source on Rates and Selectivity of m-Cresol Hydrodeoxygenation. *ACS Catal.* **2017**, *7*, 1113–1122.
(32) Sullivan, M. M.; Chen, C.-J.; Bhan, A. Catalytic Deoxygenation on Transition Metal Carbide Catalysts. *Catal. Sci. Technol.* **2016**, *6*, 602–616.
(33) Choi, J.-S.; Krafft, J.-M.; Krzton, A.; Djéga-Mariadassou, G. Study of Residual Oxygen Species over Molybdenum Carbide Prepared During In Situ DRIFTS Experiments. *Catal. Lett.* **2002**, *81*, 175–180.
(34) Lyu, S.; Wang, L.; Li, Z.; Yin, S.; Chen, J.; Zhang, Y.; Li, J.; Wang, Y. Stabilization of ε-iron Carbide as High-temperature Catalyst under Realistic Fischer–Tropsch Synthesis Conditions. *Nat. Commun.* **2020**, *11*, No. 6219.
(35) Führer, M.; van Haasterecht, T.; Bitter, J. H. Molybdenum and tungsten carbides can shine too. *Catal. Sci. Technol.* **2020**, *10*, 6089–6097.
(36) Chaffee, A. L.; Campbell, I.; Valentine, N. Sulfur Poisoning of Fischer-Tropsch Synthesis Catalysts in a Fixed-Bed Reactor. *Appl. Catal.* **1989**, *47*, 253–276.
(37) Park, K. Y.; Seo, W. K.; Lee, J. S. Selective Synthesis of Light Olefins from Syngas over Potassium-Promoted Molybdenum Carbide Catalysts. *Catal. Lett.* **1991**, *11*, 349–356.
(38) Logan, M.; Gellman, A.; Somorjai, G. A. Hydrogenation of Carbon Monoxide on Mo(100) Single Crystals and Polycrystalline Foils. *J. Catal.* **1985**, *94*, 60–68.
(39) Meng, L.; Pokochueva, E. V.; Chen, Z.; Fedorov, A.; Viñes, F.; Illas, F.; Koptyug, I. V. Contrasting Metallic (Rh^0) and Carbidic (2D-Mo_2C MXene) Surfaces in Olefin Hydrogenation Provides Insights on the Origin of the Pairwise Hydrogen Addition. *ACS Catal.* **2024**, *14*, 12500–12511.

Downloaded from pubs.acs.org/acscatsc/article-pdf/16/15/14328/6529852/cs-2026-018095.pdf by LINKOPING UNIV user on 04 October 2026

https://doi.org/10.1021/acscatal.6c01809
ACS Catal. 2026, 16, 14328–14346

(40) Schaidle, J. A.; Thompson, L. T. Fischer–Tropsch Synthesis over Early Transition Metal Carbides and Nitrides: CO Activation and Chain Growth. *J. Catal.* **2015**, *329*, 325–334.
(41) Saito, M.; Anderson, R. B. The Activity of Several Molybdenum Compounds for the Methanation of CO. *J. Catal.* **1980**, *63*, 438–446.
(42) Kountoupi, E.; Barrios, A. J.; Chen, Z.; Müller, C. R.; Ordomsky, V. V.; Comas-Vives, A.; Fedorov, A. The Impact of Oxygen Surface Coverage and Carbidic Carbon on the Activity and Selectivity of Two-Dimensional Molybdenum Carbide (2D-Mo_2C) in Fischer–Tropsch Synthesis. *ACS Catal.* **2024**, *14*, 1834–1845.
(43) Patterson, P. M.; Das, T. K.; Davis, B. H. Carbon Monoxide Hydrogenation over Molybdenum and Tungsten Carbides. *Appl. Catal., A* **2003**, *251*, 449–455.
(44) Tatsumi, T.; Muramatsu, A.; Fukunaga, T.; Tominaga, H.-o. Effects of Mo Precursors on the Activity of Alkali-Promoted Mo catalysts for Alcohol Synthesis from CO-H_2. *Polyhedron* **1986**, *5*, 257–260.
(45) Ranhotra, G. S.; Haddix, G. W.; Bell, A. T.; Reimer, J. A. Catalysis over Molybdenum Carbides and Nitrides: I. Catalyst Characterization. *J. Catal.* **1987**, *108*, 24–39.
(46) Leary, K. J.; Michaels, J. N.; Stacy, A. M. Carbon and Oxygen Atom Mobility During Activation of Mo_2C Catalysts. *J. Catal.* **1986**, *101*, 301–313.
(47) VahidMohammadi, A.; Rosen, J.; Gogotsi, Y. The World of Two-Dimensional Carbides and Nitrides (MXenes). *Science* **2021**, *372*, No. eabf1581.
(48) Naguib, M.; Mochalin, V. N.; Barsoum, M. W.; Gogotsi, Y. 25th Anniversary Article: MXenes: a New Family of Two-Dimensional Materials. *Adv. Mater.* **2014**, *26*, 992–1005.
(49) Halim, J.; Kota, S.; Lukatskaya, M. R.; Naguib, M.; Zhao, M.-Q.; Moon, E. J.; Pitock, J.; Nanda, J.; May, S. J.; Gogotsi, Y.; et al. Synthesis and Characterization of 2D Molybdenum Carbide (MXene). *Adv. Funct. Mater.* **2016**, *26*, 3118–3127.
(50) Kountoupi, E.; Piankova, D.; Agrachev, M.; Chen, Z.; Garbujo, A.; Abdala, P. M.; Müller, C. R.; Fedorov, A. Multilayered Molybdenum Carbonitride MXene: Reductive Defunctionalization, Thermal Stability, and Catalysis of Ammonia Synthesis and Decomposition. *Mater. Today Catal.* **2025**, *8*, No. 100085.
(51) Benchakar, M.; Loupias, L.; Garnero, C.; Bilyk, T.; Morais, C.; Canaff, C.; Guignard, N.; Morisset, S.; Pazniak, H.; Hurand, S.; et al. One MAX Phase, Different MXenes: A Guideline to Understand the Crucial Role of Etching Conditions on $Ti_3C_2T_x$ Surface Chemistry. *Appl. Surf. Sci.* **2020**, *530*, No. 147209.
(52) Deeva, E. B.; Kurlov, A.; Abdala, P. M.; Lebedev, D.; Kim, S. M.; Gordon, C. P.; Tsoukalou, A.; Fedorov, A.; Müller, C. R. In Situ XANES/XRD Study of the Structural Stability of Two-Dimensional Molybdenum Carbide Mo_2CT_x: Implications for the Catalytic Activity in the Water–Gas Shift Reaction. *Chem. Mater.* **2019**, *31*, 4505–4513.
(53) Sfeir, A.; Shuck, C. E.; Fadel, A.; Marinova, M.; Vezin, H.; Dacquin, J.-P.; Gogotsi, Y.; Royer, S.; Laassiri, S. Unlocking the Potential of MXene in Catalysis: Decorated Mo_2CT_x Catalyst for Ammonia Synthesis under Mild Conditions. *J. Am. Chem. Soc.* **2024**, *146*, 20033–20044.
(54) Zhou, Y.; Liang, L.; Wang, C.; Sun, F.; Zheng, L.; Qi, H.; Wang, B.; Wang, X.; Au, C.-t.; Wang, J.; et al. Precious-Metal-Free Mo-MXene Catalyst Enabling Facile Ammonia Synthesis Via Dual Sites Bridged by H-Spillover. *J. Am. Chem. Soc.* **2024**, *146*, 23054–23066.
(55) Croisé, C.; Courtois, X.; Célérier, S.; Loupias, L.; Canaff, C.; Rousseau, J.; Bion, N.; Can, F. (Ru-)Mo_2C (MXene) Catalysts for Ammonia Synthesis: From Haber-Bosch to Chemical Looping Processes. *Mater. Today Catal.* **2024**, *7*, No. 100066.
(56) Zhou, H.; Chen, Z.; Kountoupi, E.; Tsoukalou, A.; Abdala, P. M.; Florian, P.; Fedorov, A.; Müller, C. R. Two-Dimensional Molybdenum Carbide 2D-Mo_2C as a Superior Catalyst for CO_2 Hydrogenation. *Nat. Commun.* **2021**, *12*, No. 5510.
(57) Hu, Y.; Cai, J.; Shen, G.; Zhao, Z.; Liu, Y.; Liu, S.; Tu, S.; Tian, Y.; Lu, H.; Wang, J.; et al. Selective Hydrogenolysis of Biomass-Derived Aromatic Alcohols over 2D-Mo_2CO_x MXene by a Reversible Redox-Relay Mechanism. *Angew. Chem., Int. Ed.* **2025**, *64*, No. e202500881.
(58) Kärger, J.; Ruthven, D. M.; Valiullin, R. Diffusion in Nanopores: Inspecting the Grounds. *Adsorption* **2021**, *27*, 267–281.
(59) Hong, J.; Jin, C.; Yuan, J.; Zhang, Z. Atomic Defects in Two-Dimensional Materials: From Single-Atom Spectroscopy to Functionalities in Opto-/Electronics, Nanomagnetism, and Catalysis. *Adv. Mater.* **2017**, *29*, No. 1606434.
(60) Xie, C.; Yan, D.; Li, H.; Du, S.; Chen, W.; Wang, Y.; Zou, Y.; Chen, R.; Wang, S. Defect Chemistry in Heterogeneous Catalysis: Recognition, Understanding, and Utilization. *ACS Catal.* **2020**, *10*, 11082–11098.
(61) Kumar, S.; Adabasi, G.; Baykara, M. Z.; Martini, A. Modulating the Electronic Properties of Orthorhombic Mo_2C Surfaces with Strain and Defects: Insights from First-Principles Calculations. *J. Phys. Chem. C* **2025**, *129*, 369–378.
(62) Brazdil, J. F.; Glaeser, L. C.; Grasselli, R. K. An investigation of the role of bismuth and defect cation vacancies in selective oxidation and ammoxidation catalysis. *J. Catal.* **1983**, *81*, 142–146.
(63) Tao, Q.; Dahlqvist, M.; Lu, J.; Kota, S.; Meshkian, R.; Halim, J.; Palisaitis, J.; Hultman, L.; Barsoum, M. W.; Persson, P. O. Å.; et al. Two-Dimensional $Mo_{1.33}C$ MXene with Divacancy Ordering Prepared from Parent 3D Laminate with In-plane Chemical Ordering. *Nat. Commun.* **2017**, *8*, No. 14949.
(64) Lind, H.; Halim, J.; Simak, S. I.; Rosen, J. Investigation of Vacancy-Ordered $Mo_{1.33}C$ MXene from First Principles and X-ray Photoelectron Spectroscopy. *Phys. Rev. Mater.* **2017**, *1*, No. 044002.
(65) Halim, J.; Palisaitis, J.; Lu, J.; Thörnberg, J.; Moon, E. J.; Precner, M.; Eklund, P.; Persson, P. O. Å.; Barsoum, M. W.; Rosen, J. Synthesis of Two-Dimensional $Nb_{1.33}C$ (MXene) with Randomly Distributed Vacancies by Etching of the Quaternary Solid Solution $(Nb_{2/3}Sc_{1/3})_2AlC$ MAX Phase. *ACS Appl. Nano Mater.* **2018**, *1*, 2455–2460.
(66) Zhang, H.; Hu, T.; Sun, W.; Hu, M.; Cheng, R.; Wang, X. Atomic Repartition in MXenes by Electron Probes. *Chem. Mater.* **2019**, *31*, 4385–4391.
(67) Célérier, S.; Hurand, S.; Garnero, C.; Morisset, S.; Benchakar, M.; Habrioux, A.; Chartier, P.; Mauchamp, V.; Findling, N.; Lanson, B.; et al. Hydration of $Ti_3C_2T_x$ MXene: An Interstratification Process with Major Implications on Physical Properties. *Chem. Mater.* **2019**, *31*, 454–461.
(68) Biscoe, J.; Warren, B. E. An X-Ray Study of Carbon Black. *J. Appl. Phys.* **1942**, *13*, 364–371.
(69) Liu, J.; Yu, L.; Hu, E.; Guiton, B. S.; Yang, X.-Q.; Page, K. Large-Scale Synthesis and Comprehensive Structure Study of δ-MnO_2. *Inorg. Chem.* **2018**, *57*, 6873–6882.
(70) Ehlsissen, K. T.; Delahaye-Vidal, A.; Genin, P.; Figlarz, M.; Willmann, P. Preparation and Characterization of Turbostratic Ni/Al Layered Double Hydroxides for Nickel Hydroxide Electrode Applications. *J. Mater. Chem.* **1993**, *3*, 883–888.
(71) Faure, C.; Delmas, C.; Fouassier, M. Characterization of a turbostratic α-nickel hydroxide quantitatively obtained from an $NiSO_4$ solution. *J. Power Sources* **1991**, *35*, 279–290.
(72) Holland, K. L.; Walker, J. R. Crystal Structure Modeling of a Highly Disordered Potassium Birnessite. *Clays Clay Miner.* **1996**, *44*, 744–748.
(73) Halim, J.; Etman, A. S.; Elsukova, A.; Polcik, P.; Palisaitis, J.; Barsoum, M. W.; Persson, P. O. Å.; Rosen, J. Tailored synthesis approach of $(Mo_{2/3}Y_{1/3})_2AlC$ *i*-MAX and its two-dimensional derivative $Mo_{1.33}CT_z$ MXene: enhancing the yield, quality, and performance in supercapacitor applications. *Nanoscale.* **2021**, *13*, 311–319.
(74) Urbankowski, P.; Anasori, B.; Hantanasirisakul, K.; Yang, L.; Zhang, L.; Haines, B.; May, S. J.; Billinge, S. J. L.; Gogotsi, Y. 2D Molybdenum and Vanadium Nitrides Synthesized by Ammoniation of 2D Transition Metal Carbides (MXenes). *Nanoscale* **2017**, *9*, 17722–17730.

Downloaded from pubs.acs.org/acscatal/article-pdf/16/15/14328/6529852/cs-2026-018095.pdf by LINKOPING UNIV user on 04 October 2026

(75) Meshkian, R.; Näslund, L.-Å.; Halim, J.; Lu, J.; Barsoum, M. W.; Rosen, J. Synthesis of Two-Dimensional Molybdenum Carbide, Mo_2C, from the Gallium Based Atomic Laminate Mo_2Ga_2C. *Scripta Mater.* **2015**, *108*, 147–150.
(76) Brette, F.; Célérier, S.; Canaff, C.; Loupias, L.; Paris, M.; Habrioux, A.; Boucher, F.; Mauchamp, V. XPS Binding Energy Shifts in 2D $Ti_3C_2T_z$ MXene go largely Beyond Intuitive Explanations: Rationalization from DFT Simulations and Experiments. *Small Methods* **2025**, *9*, No. 2400848.
(77) Hwang, J. H.; Kim, D. H.; Kang, J. S.; Kolesnik, S.; Chmaissem, O.; Mais, J.; Dabrowski, B.; Baik, J.; Shin, H. J.; Lee, J.; et al. Soft x-ray absorption spectroscopy study of Mo-rich $SrMn_{1-x}Mo_xO_3$ ($x \geqslant 0.5$). *Phys. Rev. B* **2011**, *83*, No. 073103.
(78) Chen, J. G.; Eng, J.; Kelty, S. P. NEXAFS Determination of Electronic and Catalytic Properties of Transition Metal Carbides and Nitrides: From Single Crystal Surfaces to Powder Catalysts. *Catal. Today* **1998**, *43*, 147–158.
(79) Kapoor, R.; Oyama, S. T.; Friihberger, B.; DeVries, B. D.; Chen, J. G. Characterization of Early Transition Metal Carbides and Nitrides by NEXAFS. *Catal. Lett.* **1995**, *34*, 179–189.
(80) Chen, J. G. NEXAFS investigations of transition metal oxides, nitrides, carbides, sulfides and other interstitial compounds. *Surf. Sci. Rep.* **1997**, *30*, 1–152.
(81) Chen, J. G.; Frühberger, B.; Eng, J.; Bent, B. E. Controlling Surface Reactivities of Transition Metals by Carbide Formation. *J. Mol. Catal. A: Chem.* **1998**, *131*, 285–299.
(82) Yu, C. C.; Ramanathan, S.; Dhandapani, B.; Chen, J. G.; Oyama, S. T. Bimetallic Nb–Mo Carbide Hydroprocessing Catalysts: Synthesis, Characterization, and Activity Studies. *J. Phys. Chem. B* **1997**, *101*, 512–518.
(83) Soriano, L.; Abbate, M.; Vogel, J.; Fuggle, J. C.; Fernández, A.; González-Elipe, A. R.; Sacchi, M.; Sanz, J. M. The Electronic Structure of Mesoscopic NiO Particles. *Chem. Phys. Lett.* **1993**, *208*, 460–464.
(84) Amargianou, F.; Bärmann, P.; Shao, H.; Taberna, P.-L.; Simon, P.; Gonzalez-Julian, J.; Weigand, M.; Petit, T. Nanoscale Surface and Bulk Electronic Properties of $Ti_3C_2T_x$ MXene Unraveled by Multimodal X-Ray Spectromicroscopy. *Small Methods* **2024**, *8*, No. 2400190.
(85) Wang, D.; Su, D. S.; Schlögl, R. Electron Beam Induced Transformation of MoO_3 to MoO_2 and a New Phase MoO. *Z. Anorg. Allg. Chem.* **2004**, *630*, 1007–1014.
(86) Wu, G.; Sekiguchi, T.; Baba, Y.; Shimoyama, I. X-ray Absorption Fine Structure and Photon-Stimulated Ion Desorption from Solid MoO_3 at Molybdenum $3p_{1/2}$, $3p_{3/2}$ and oxygen 1*s* edges. *Nucl. Instrum. Methods Phys. Res., Sect. B* **2006**, *245*, 406–410.
(87) Frati, F.; Hunault, M. O. J. Y.; de Groot, F. M. F. Oxygen K-edge X-ray Absorption Spectra. *Chem. Rev.* **2020**, *120*, 4056–4110.
(88) Cramer, S. P.; Eccles, T. K.; Kutzler, F. W.; Hodgson, K. O.; Mortenson, L. E. Molybdenum X-Ray Absorption Edge Spectra. The Chemical State of Molybdenum in Nitrogenase. *J. Am. Chem. Soc.* **1976**, *98*, 1287–1288.
(89) Martens, G.; Rabe, P.; Wenck, P. Destructive Interference and Multiple Scattering Effects Observed in Ca K-Edge EXAFS Spectra. *Phys. Status Solidi A* **1985**, *88*, 103–111.
(90) Michalowicz, A.; Verdaguer, M.; Mathey, Y.; Clement, R. Order and Disorder in Low Dimensional Materials: Beyond the First Coordination Sphere with EXAFS. In *Synchrotron Radiation in Chemistry and Biology I*, Vol *145; Springer: Berlin, Heidelberg*, **1988**.
(91) Zhang, J.; Wu, X.; Cheong, W.-C.; Chen, W.; Lin, R.; Li, J.; Zheng, L.; Yan, W.; Gu, L.; Chen, C.; et al. Cation Vacancy Stabilization of Single-Atomic-Site $Pt_1/Ni(OH)_x$ Catalyst for Diboration of Alkynes and Alkenes. *Nat. Commun.* **2018**, *9*, No. 1002.
(92) Kuznetsov, D. A.; Chen, Z.; Kumar, P. V.; Tsoukalou, A.; Kierzkowska, A.; Abdala, P. M.; Safonova, O. V.; Fedorov, A.; Müller, C. R. Single Site Cobalt Substitution in 2D Molybdenum Carbide (MXene) Enhances Catalytic Activity in the Hydrogen Evolution Reaction. *J. Am. Chem. Soc.* **2019**, *141*, 17809–17816.
(93) Sharma, N.; Godeffroy, L.; Bärmann, P.; Amargianou, F.; Weisser, A.; Dessoliers, Z.; Lounasvuori, M.; Weigand, M.; Petit, T. Nanoscale chemical imaging of pseudocapacitive charge storage in MXenes. *Energy Environ. Sci.* **2026**, *19*, 680–690.
(94) Soriano, L.; Gutiérrez, A.; Preda, I.; Palacín, S.; Sanz, J. M.; Abbate, M.; Trigo, J. F.; Vollmer, A.; Bressler, P. R. Splitting of Ni 3*d* States at the Surface of NiO Nanostructures. *Phys. Rev. B* **2006**, *74*, No. 193402.
(95) Walder, B. J.; Schorr, N. B.; Brunke, L. B.; Siegal, M. P.; Alam, T. M.; Fritzsching, K. J.; Lambert, T. N. Composites of $(C_4F)_n$ and $(CF)_n$ Synthesized by Uncatalyzed Fluorination of Graphite. *Solids* **2022**, *3*, 237–257.
(96) Kuznetsov, D. A.; Chen, Z.; Abdala, P. M.; Safonova, O. V.; Fedorov, A.; Müller, C. R. Single-Atom-Substituted Mo_2CT_x:Fe-Layered Carbide for Selective Oxygen Reduction to Hydrogen Peroxide: Tracking the Evolution of the MXene Phase. *J. Am. Chem. Soc.* **2021**, *143*, 5771–5778.
(97) Hart, J. L.; Hantanasirisakul, K.; Lang, A. C.; Anasori, B.; Pinto, D.; Pivak, Y.; van Omme, J. T.; May, S. J.; Gogotsi, Y.; Taheri, M. L. Control of MXenes' Electronic Properties Through Termination and Intercalation. *Nat. Commun.* **2019**, *10*, No. 522.
(98) Parthé, E.; Sadogopan, V. The Structure of Dimolybdenum Carbide by Neutron Diffraction Technique. *Acta Crystallogr.* **1963**, *16*, 202–205.
(99) Page, K.; Li, J.; Savinelli, R.; Szumila, H. N.; Zhang, J.; Stalick, J. K.; Proffen, T.; Scott, S. L.; Seshadri, R. Reciprocal-Space and Real-Space Neutron Investigation of Nanostructured Mo_2C and WC. *Solid State Sci.* **2008**, *10*, 1499–1510.
(100) Jaumot, J.; Gargallo, R.; de Juan, A.; Tauler, R. A Graphical User-Friendly Interface for MCR-ALS: a New Tool for Multivariate Curve Resolution in MATLAB. *Chemom. Intell. Lab. Syst.* **2005**, *76*, 101–110.
(101) de Juan, A.; Jaumot, J.; Tauler, R. Multivariate Curve Resolution (MCR) Solving the Mixture Analysis Problem. *Anal. Methods* **2014**, *6*, 4964–4976.
(102) Jaumot, J.; de Juan, A.; Tauler, R. MCR-ALS GUI 2.0: New Features and Applications. *Chemom. Intell. Lab. Syst.* **2015**, *140*, 1–12.
(103) Figueroa, S. J. A.; Prestipino, C. PrestoPronto: a Code Devoted to Handling Large Data Sets. *J. Phys: Conf. Ser.* **2016**, *712*, No. 012012.
(104) Lee, J. S.; Yie, J. E. An XANES study of carbides of molybdenum and tungsten. *Korean J. Chem. Eng.* **1991**, *8*, 164–167.
(105) Yao, S.; Zhang, X.; Zhou, W.; Gao, R.; Xu, W.; Ye, Y.; Lin, L.; Wen, X.; Liu, P.; Chen, B.; et al. Atomic-layered Au Clusters on α-MoC as Catalysts for the Low-Temperature Water-Gas Shift Reaction. *Science* **2017**, *357*, 389–393.
(106) Sun, X.; Yu, J.; Cao, S.; Zimina, A.; Sarma, B. B.; Grunwaldt, J.-D.; Xu, H.; Li, S.; Liu, Y.; Sun, J. In Situ Investigations on Structural Evolutions During the Facile Synthesis of Cubic α-MoC_{1-x} Catalysts. *J. Am. Chem. Soc.* **2022**, *144*, 22589–22598.
(107) Baddour, F. G.; Roberts, E. J.; To, A. T.; Wang, L.; Habas, S. E.; Ruddy, D. A.; Bedford, N. M.; Wright, J.; Nash, C. P.; Schaidle, J. A.; et al. An Exceptionally Mild and Scalable Solution-Phase Synthesis of Molybdenum Carbide Nanoparticles for Thermocatalytic CO_2 Hydrogenation. *J. Am. Chem. Soc.* **2020**, *142*, 1010–1019.
(108) Jin, S.; Guo, Y.; Wang, J.; Wang, L.; Hu, Q.; Zhou, A. Carbon dioxide adsorption of two-dimensional Mo_2C MXene. *Diamond Relat. Mater.* **2022**, *128*, No. 109277.
(109) Amagbor, S. C.; Maruf, A. A.; Adesope, Q.; Khan, M. H.; R Mudiyanselage, R.; Pudasaini, A.; Ashrafian, A.; Dhungana, M.; Sonnier, K.; Chen, L.; et al. Effects of Nonstoichiometry on the Ambient Oxidation of Cubic Mo_2C and Impact on CO Hydrogenation. *J. Phys. Chem. C* **2026**, *130*, 942–952.
(110) Huheey, J. E. *Inorganic Chemistry: Principles of Structure and Reactivity:* 2nd ed; Harper, **1978**, p. 360.
(111) Berger, R.; Bissey, J.-C.; Kliava, J.; Daubric, H.; Estournès, C. Temperature Dependence of Superparamagnetic Resonance of Iron Oxide Nanoparticles. *J. Magn. Magn. Mater.* **2001**, *234*, 535–544.

Downloaded from pubs.acs.org/acscats/article-pdf/16/15/14328/6529852/cs-2026-018095.pdf by LINKOPING UNIV user on 04 October 2026

https://doi.org/10.1021/acscatal.6c01809
ACS Catal. 2026, 16, 14328–14346

(112) Chen, J. G. Carbide and Nitride Overlayers on Early Transition Metal Surfaces: Preparation, Characterization, and Reactivities. *Chem. Rev.* **1996**, *96*, 1477–1498.
(113) Evans, J.; Mosselmans, J. F. W. L-edge Studies on Molybdenum. *J. Phys. Chem.* **1991**, *95*, 9673–9676.
(114) Mo, T.; Xu, J.; Yang, Y.; Li, Y. Effect of Carburization Protocols on Molybdenum Carbide Synthesis and Study on its Performance in CO Hydrogenation. *Catal. Today* **2016**, *261*, 101–115.
(115) Li, S.; Krishnamoorthy, S.; Li, A.; Meitzner, G. D.; Iglesia, E. Promoted Iron-Based Catalysts for the Fischer–Tropsch Synthesis: Design, Synthesis, Site Densities, and Catalytic Properties. *J. Catal.* **2002**, *206*, 202–217.
(116) Khodakov, A. Y.; Chu, W.; Fongarland, P. Advances in the Development of Novel Cobalt Fischer–Tropsch Catalysts for Synthesis of Long-Chain Hydrocarbons and Clean Fuels. *Chem. Rev.* **2007**, *107*, 1692–1744.
(117) Wang, L.; Wang, H.; Huang, H.; Yun, T.; Song, C.; Shi, C. Transition Metal Carbides: Emerging CO_2 Hydrogenation Catalysts, from Recent Advance to Future Exploration. *Adv. Funct. Mater.* **2024**, *34*, No. 2309850.
(118) de Smit, E.; Weckhuysen, B. M. The Renaissance of Iron-based Fischer–Tropsch Synthesis: on the Multifaceted Catalyst Deactivation Behaviour. *Chem. Soc. Rev.* **2008**, *37*, 2758–2781.

Downloaded from pubs.acs.org/acscatsc/article-pdf/16/15/14328/6529852/cs-2026-018095.pdf by LINKOPING UNIV user on 04 October 2026

https://doi.org/10.1021/acscatal.6c01809
ACS Catal. 2026, 16, 14328–14346